THESIS FOR THE DEGREE OF LICENTIATE OF ENGINEERING

Nanofluidic Scattering Microscopy for Single Particle Catalysis

BJÖRN ALTENBURGER

CHALMERS
UNIVERSITY OF TECHNOLOGY

Department of Physics

CHALMERS UNIVERSITY OF TECHNOLOGY

Gothenburg, Sweden 2022

Nanofluidic Scattering Microscopy for Single Particle Catalysis

BJÖRN ALTENBURGER

Department of Physics
Chalmers University of Technology
SE-412 96 Gothenburg
Sweden
Telephone + 46 (0)31-772 1000

Cover:
Artistic rendering of a nanochannel containing a trapped colloidal nanoparticle in front of a constriction. A catalytic reaction causes the formation of smaller bubbles that combine into a large bubble that fills the channel opposite the particle.

Printed at Chalmers Reproservice

Gothenburg, Sweden 2022

Nanofluidic Scattering Microscopy for Single Particle Catalysis

Björn Altenburger
Department of Physics
Chalmers University of Technology

Abstract

Heterogeneous catalysis concerns material formulations – catalysts – that can assist a chemical reaction by improving its rate or selectivity, by lowering activation barriers and altering the energy landscape. The core of catalysts are often tiny metal particles that provide a large reaction surface at a small volume, as well as low coordination sites whose type and abundance depends on particle size and shape. Hence, such nanoparticles come in a broad spectrum of sizes and shapes when studied in a so-called ensemble comprised of millions of particles. Ensemble experimental techniques therefore often disregard the structural heterogeneity of nanoparticles as the measurements of such samples provide information on the averaged response of the heterogeneous ensemble. Consequently, "superparticles" with exceptional performance may be overlooked, or erroneous structure-function correlations may be established.

To overcome the ensemble averaging problem, various techniques for single particle catalysis have been developed. The approaches include methods like fluorescence microscopy, X-ray diffraction and scattering, electron microscopy and plasmonic sensing. These methods have in common that they detect electrons or photons that report either on the reactant molecules consumed, the product molecules formed, changes to the catalyst particle itself, or temperature changes that the reaction evokes in the particle surrounding. However, none of the experimental methods provide direct single particle activity information without either using plasmonic enhancement effects that may also impact the studied reaction itself and limit the range of catalyst materials that can be studied or using fluorescence that limits reaction conditions to ultralow concentrations and to a narrow range of reactions.

The overarching goal of the work presented in this thesis has been to develop an optical microscopy technique that can quantitatively measure catalytic activity, and in the longer term even selectivity, of a single nanoparticle without the limitations of existing single particle methods. At the core of this method that we call Nanofluidic Scattering Microscopy are nanofluidic channels that can accurately control the transport of reagents to and from a single catalytically active particle localized inside the channels. As a second key trait, the unique light scattering properties of nanochannels render them highly sensitive to refractive index changes of the fluid inside them. Hence, when a catalytic reaction alters the molecular composition of the fluid in the channel, its light scattering characteristics change and reveal in this way the catalytic performance of the nanoparticle.

In this thesis, I describe my winding journey towards the first successful implementation of Nanofluidic Scattering Microscopy, where I characterize the catalytic activity in terms of turnover frequency of single colloidal Pt nanoparticles trapped inside nanofluidic channels during the H_2O_2 decomposition reaction. The experiments reveal that ligands covering the particle surface distinctly impact the activity.

List of appended papers

This thesis is the basis for the work presented in the following papers:

Paper I

Nanofluidic Scattering Microscopy of Single Colloidal Platinum Nanoparticle H_2O_2 Decomposition Catalysis

Björn Altenburger, Carl Andersson, Sune Levin, Fredrik Westerlund, Joachim Fritzsche, and Christoph Langhammer

In Manuscript

Table of contents

1 Introduction 1
2 Nanofluidic Scattering Microscopy 7
2.1 The original idea 7
2.1.1 Basics of Mie-Scattering 7
2.1.2 The Kramers-Kronig relation 13
2.2 Nanofabrication of fluidic chips 14
2.3 The microscope setup and first results 17
2.3.1 The setup 17
2.3.2 Wavelength-resolved scattering intensity measurements of transparent liquids 19
2.3.3 Nanofluidic Scattering Spectroscopy of a Brilliant Blue solution 22
2.4 Setup and nanofluidic chip refinement towards single particle catalysis 24
2.4.1 First stage of refinements 24
2.4.2 Second Stage of refinements 29
2.5 Fluidic system clogging by debris particles 37
2.6 Investigating low Pd nanoparticle catalytic activity 39
3 A new start 41
3.1 A simplified chip design optimized for colloidal particle trapping 41
3.2 Trapping colloidal Pt nanoparticles in nanochannels 42
3.3 Summary of the appended manuscript 45
4 Summary and Conclusions 47
5 Outlook 49
6 Acknowledgements 51
7 References 53

1 Introduction

The challenge I have targeted in this thesis is to study catalytic reactions on nanoparticles in realistic conditions without the use of fluorescence or nanoplasmonic techniques. Is this an important task? In heterogeneous catalysis, the best catalyst for a specific chemical reaction is found when the highest reactivity or most advantageous selectivity is obtained with the least amount of catalyst used. To this end, since heterogeneous catalytic reactions take place on the surface of a catalyst in the solid state, the ratio of surface versus volume of that catalyst is maximized when using small nanoparticles in the sub-10 nm size range that extends all the way down to so-called clusters comprised of tens of atoms or even single atoms, as the most extreme case. However, it is not only size but also particle shape that matters, since certain reactions, for example, prefer corner or edge sites on the particles[1], while some prefer certain crystalline planes[2] and for some reactions, it is the very specific interplay between different types of sites[3] that is key. However, when nanoparticles are produced, they usually exhibit a significant variety in terms of their shape and size, as well as composition if alloys are considered. Hence, if one would like to experimentally correlate catalyst reactivity with particle size, shape and composition, to not average out potentially relevant structural effects, it is beneficial to investigate catalyst nanoparticles individually. This, however, is a significant experimental challenge due to their tiny size and due to the tiny amount of product molecules produced on their surface.

The challenge to study catalytic reactions over single particles has inspired many scientists over the years and the various experimental approaches are a result of a long tradition in heterogeneous catalysis where one tries to reveal the details of a surface reaction while the catalyst is working in real reaction conditions[4–9]. The term “in situ” is used in this context to describe methods that can characterize catalysts in controlled environments, although such conditions may not represent the environments the catalyst will experience under operation conditions. The term “operando” goes one step further and is used for approaches that monitor the catalyst while it is converting reactants. As the relevant length scales in catalysis are in the micro and nanometer regime, the experimental techniques used to study catalysts have also entered this realm. The entry point to this nanoscopic environment is for many approaches synchrotron radiation as the short wavelength can resolve very small structures[10] (10 nm to 5 nm) while the generated photons can penetrate the reactor atmosphere and the catalyst. Examples of widely used synchrotron-based techniques are scanning-transmission X-ray microscopy (STXM) and quick scan X-ray absorption fine structure (QXAFS)[11,12]. Being based on highly transmissive X-rays, using these methods the inner structure of catalysts can be revealed with nanometer spatial resolution tiny pores and the metal nanoparticle distribution inside can be resolved[12]. The drawback with synchrotron methods is the extensive infrastructure that is needed to generate the radiation and that they reveal only the structure of the catalyst but often not their activity at the same time. Another noteworthy example of an experimental method for single particle catalysis is using the fluorescence emission of (single) molecules[13] to reveal chemical reactions on the surface of single nanoparticles, sometimes even

with sub-particle spatial resolution[6,14–16]. This approach is relatively new to chemistry but has been used in biology for decades[13] to study the processes within cells and organelles and earned Stefan Hell the Nobel prize in 2014. While the experimental setup required is relatively simple compared to a synchrotron experiment, the main limiting factors for (super resolution) fluorescence microscopy in single particle catalysis are that one is limited to a very small number specific reactions that either form a fluorescent product or during which fluorescence is extinct. Furthermore, one has to work at a from a practical perspective unrealistically low reactant concentration to ensure single molecular resolution in the super resolution version of fluorescence microscopy.

Another family of single particle catalysis experimental techniques focuses on the nanoparticles themselves. To this end, when talking about nanoparticles in heterogeneous catalysis, they are usually only regarded as the catalytically active part and therefore the entities of interest to be investigated. However, it turns out that they also - at the same time - can play the part of the observer of a catalytic process that takes place on their surface[17]. This is enabled by an optical phenomenon called localized surface plasmon resonance (LSPR)[17–19], a coherent collective oscillation of the electrons of the particle that has its resonance frequency in the UV-vis-NIR spectral range, depending on the size, shape and composition of the particle, as well as the particles' intimate surroundings. As the resonance frequency of the LSPR therefore is sensitive to, for example, the oxidation state of a metal nanoparticle, it can be used to monitor the surface state of single catalyst nanoparticles in situ[18,20–22] by tracking shifts in resonance frequency with high precision[23] at the level of single nanoparticles using dark-field scattering microscopy[17,24]. However, this plasmonic nanospectroscopy and imaging concept falls short on being able to also provide information about the activity of the catalyst particle. In an attempt to alleviate this problem, earlier work in our group has combined LSPR with quadrupole mass spectrometry from particles localized in tiny nanofluidic reactors[18,20,21]. However, the QMS readout is limited to a few hundred nanoparticles since it does not provide the sensitivity to address individual ones, thereby still leaving the "holy grail" of an activity measurement from a single nanoparticle in operando at technically relevant conditions an unreached dream.

The plasmon oscillation of metal nanoparticles can also be used to enhance the Raman absorption of molecules in their close vicinity, as it is done in, so-called, plasmon or tip enhanced Raman spectroscopy (PERS and TERS, respectively)[25,26] that has been used to investigate the photocatalytic processes of nitrothiophenol on gold surfaces[27]. One of the main drawbacks and limitations of PERS and TERS is that the enhancing plasmonic particle or tip also must serve as the catalyst, which limits the catalyst materials available severely since essentially only Ag and Au would provide a strong enough Raman-enhancing effect. To overcome this limitation, a solution was developed where the Raman-enhancing (Au) nanoparticle is isolated by a passive shell, in analogy to indirect nanoplasmonic sensing[22,28], in what has come to be known as Shell-Isolated Nanoparticle-Enhanced Raman Spectroscopy (SHINERS)[11]. This method has for example been successfully used for the investigation of the oxygen reduction reaction on high-index Pt where evidence of OH and OOH intermediates was found[29]. Despite this significant advance SHINERS has provided to Raman-based single particle catalysis, it is still limited by the fact that a passive and bulky (compared to the catalyst particles) observer nanoparticle must be used, which may quite significantly impact the catalyst formulation and thus potentially the catalytic properties. Furthermore, SHINERS-type

"antenna-reactor complexes", where a plasmonic antenna is placed close to catalyst nanoparticles, are widely explored in plasmon-mediated catalysis to enhance and steer catalytic reactions by light[30–33]. This highlights a further risk of plasmon enhanced Raman spectroscopy methods, that is, that the plasmonic effect used to probe the catalytic reaction at the same time also might (dramatically) impact it and therefore lead to wrong conclusions.

Another class of experimental methods widely used to investigate catalysis at the single nanoparticle level are electron microscopy approaches[7,10,34,35]. These methods focus on elucidating the (dynamics of) catalyst particle structure and (oxidation) state and offer atomic resolution under certain conditions. At the early stages, scanning electron microscopy (SEM) and transmission electron microscopy (TEM) was used to study catalyst ex-situ, that is, before and after reaction. The development of differentially pumped microscopes, sample cells and specialized holders have enabled the operando investigation of single particles at high pressures[36–38] and even in the liquid phase[39,40]. They have, for example, revealed the oscillating behavior of Pt[41] or Pd[42] nanoparticles during reaction and monitored the dynamics of single atoms[43]. However, as the key limitations, electron microscopy methods can only investigate one particle at a time, and they do not provide information about (single particle) catalyst activity or selectivity.

This plethora of single particle catalysis characterization techniques that has been developed to date is evidence enough that we are dealing with both an interesting and highly relevant topic in heterogeneous catalysis that has sparked the interest of many research groups.

I present in this thesis my approach to address the above outlined challenges in single particle catalysis towards realizing its ultimate goal. The concept that I introduce in my work is on one hand based on the fact that the refractive index (RI) of any fluid will change if its molecular composition is changed[44], for example by a chemical reaction between constituents of the fluid. On the other hand, the concept is based on nanofluidic systems and our expertise to use them to both manipulate and control fluids and single nanoparticles at the nanoscale in the context of single particle catalysis[20,21,45–48]. Finally, it builds on our recent discovery of the unique optical properties of nanofluidic systems that enabled the label-free size and mass determination of single biomolecules using what we call Nanofluidic Scattering Microscopy[47] (NSM).

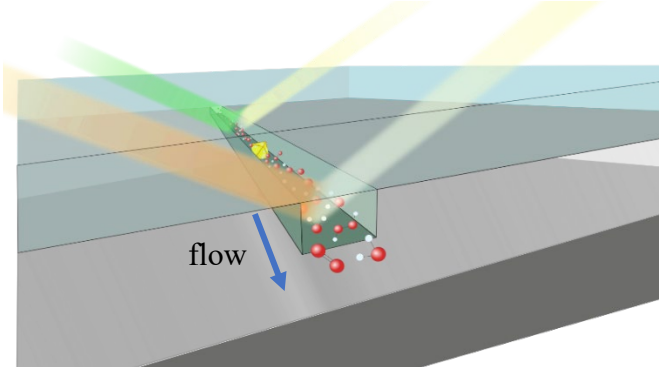

***Figure 1**. Artist's rendition of nanofluidic scattering microscopy for the monitoring of catalytic activity of a single nanoparticle localized inside a nanofluidic channel. Due to a reaction-induced refractive index difference in the liquid in the channel up- and downstream of the catalyst particle, the light scattering intensity from the channel is different in these regions and thereby enables measurements of conversion and thus particle activity.*

To this end, the method that I have developed uses the NSM principle not to detect single molecules but to track the changes in the fluid that is residing in the channel that are induced by a catalytic reaction over a surface of a single nanoparticle localized inside the channel (**Figure 1**).

Some of the key features of NSM that I will discuss in detail in the subsequent chapters are that the used nanochannels´ geometrical cross section is smaller than any wavelength of the visible light spectral range and that these channels nevertheless scatter visible light very efficiently in the Mie-regime. The scattering is owing to the RI contrast between the solid material that hosts the channels and their interior which is either a gas or a liquid. As the second key feature, I will make use of the fact that the scattering intensity of a nanochannel is strongly modulated by the RI difference between channel walls and channel interior. As the hypothesis I set out to explore is that if reactants are flushed into a nanochannel and react on a catalytically active particle localized inside the channel, the molecular structure of a sizable fraction of the molecules in the channel will be changed due to the reaction. Hence, since this molecular structure change alters the molecular polarizability and thus the RI of the liquid in the channel, the catalytic reaction is expected to induce a measurable change of the nanochannels' light scattering both in intensity and spectrum. Therefore, this will make it possible to monitor the catalytic reaction and determine its rate.

Since the NSM approach, in principle, is compatible with a wide range of reactant types and concentrations, as well as reaction pressures, it promises to enable single particle catalysis studies in technically relevant reaction conditions in operando. Furthermore, there are no boundary conditions on the reaction itself, that is, it neither needs to be fluorescent nor have a "color" and there are no plasmonic enhancement effects necessary which should dramatically lower potential artefacts induced by the used probes and enable experiments with an almost unlimited number of catalytic reactions and catalyst materials.

A second aspect is that the benefit of the nanochannels is not limited to their optical properties that enable light scattering based optical microscopy. In fact, they also provide us with unprecedented control of the reaction parameters. For one, we can isolate single particles in their respective nanochannel, such that we avoid any crosstalk between particles, e.g., via reactant concentration gradients or spill-over effects. Secondly, having arrangements of many parallel nanochannels on a chip and in the field of view of the microscope allows to study many single nanoparticles at the same time, while they all are isolated in their own nanochannel. Thirdly, the fluidic system allows us to also accurately control the flow of reactants and with that the mass transport to and from single nanoparticles. In this way, the nanochannels also function as "model pores" that mimic widely used meso- and nanoporous catalyst support materials. Finally, due to the tiny dimensions of the nanochannels, they efficiently prevent extensive dilution of (the small number of) product molecules formed on single catalyst nanoparticles and therefore see to maximizing the RI contrast induced by the reaction. This, in turn, maximizes the chance that the conversion over a single nanoparticle can be experimentally measured.

This thesis is structured in the following way: I will start by introducing the underlying physical principle of NSM for single particle catalysis applications in the beginning of the second chapter and explain the different options we have from a fundamental governing physical perspective. These theoretical predictions will subsequently be corroborated with experimental

data from first measurements in the following section, also explaining our motivation to further develop this technique. The section thereafter is then dedicated to the various ideas I have implemented and explored to both deeper understand and improve the performance of our experimental setup, including advanced nanofluidic chip designs, modifications of the darkfield microscope itself and automated data acquisition and evaluation.

The last section of the second chapter is dedicated to a summary and discussion of the challenges I have encountered during the development of NSM for single particle catalysis. I feel that it is important to discuss in detail those (sometimes still unresolved) challenges in this thesis because it is tackling and trying to resolve them that has led us to the stage we are today, and it is also what forms the basis for our understanding of what needs further improvement and what probably the ultimate limits of our technique are.

Chapter 3 therefore starts out with an analysis of what has been achieved so far and the corresponding key insights gained. On this basis, I subsequently introduce a new nanofluidic chip design and motivate the step from using nanofabricated catalyst particles to instead using colloidal nanocrystals synthesized in solution and trapped inside a nanofluidic channel at a predefined position for my experiments. The insight gained in the previous chapters is here combined with new results such that a foundation of basic understanding is established. The key point here is the emergence of gas bubbles in the nanochannels that have their origin in the catalytic reaction on the surface of a single particle. On the basis of measuring the growth rate of these bubbles in the nanochannels, I will lay out how I finally arrived at a position in the development of this technique that justified the writing of a first publication on this topic.

2 Nanofluidic Scattering Microscopy

2.1 The original idea

Scattering of electromagnetic waves from small objects is an extensive field in physics. It is often separated into the different theories that describe scattering according to the size of the scattering object. At the level of the smallest objects, it is Rayleigh-theory that is used to describe the interaction of light with atoms and molecules, both being much smaller than the wavelength of the incident light. Since this type of scattering shows a distinctive dependency on the wavelength, it leads to common phenomena, such as the blue sky and colorful red and orange sunrises. Interestingly, we also find another type of scattering occurring in the sky above us, since clouds have a distinctive white-grey color. In contrast to the rest of the atmosphere, clouds are comprised of water droplets or ice crystals with sizes comparable to the wavelengths of sunlight. In this case, it is therefore Mie-scattering that describes best the scattering of electromagnetic waves from the water particles that form clouds. Mie-theory indeed predicts a nearly equal scattering intensity for all wavelengths, which thus explains the white-grey color of clouds, as well as of milk and smoke.

In my work, I use nanofluidic channels to study catalysis on single nanoparticles since they (i) offer a unique means to isolate single nanoparticles to avoid crosstalk between them, (ii) enable nanoscale control of reactant transport to and reaction product from single nanoparticles and (iii) prevent the excessive dilution of reaction product. As an important additional point here, I note that these channels have geometrical cross sections on the same order of magnitude as the wavelengths of visible light (light is visible for the human eye between 310 nm and 1100 nm[49]) since the typical width of nanochannels I have worked with is between 100 nm and 200. Hence, they interact strongly with visible light and this interaction is the basis for the NSM concept I have used to study catalytic reactions on single nanoparticles inside nanochannels. To fundamentally understand the light scattering properties of these nanochannels, I present below a short derivation of the most important formulas based on Mie-theory that are required for this purpose. The derivation is based on the assumption that the fluid that fills the nanochannels can be described by a bulk material whose optical properties are defined by its complex dielectric function.

2.1.1 Basics of Mie-Scattering

In this section, I will describe a single nanochannel as a scattering entity when visible light is incident on it. To describe the nanochannels with rectangular cross section used in my experiments in the Mie-framework we can approximate them as infinitely long cylinders. By doing so, we can then follow the derivation of equations that describe the scattering of light from such an object provided by Bohren and Huffman[50].

At the very start, there is the description of the incoming light as an electromagnetic wave.

$$\nabla^2\psi + k^2\psi = 0 \qquad \textit{Equation 1}$$

Here, ψ is the amplitude of the wave and the wavenumber $k = \frac{\omega}{c} = \omega\sqrt{\varepsilon\mu}$. Since the channel is approximated as being cylindrical, it is useful to use cylindrical coordinates, as shown in Equation 2.

$$\frac{1}{r}\frac{\partial}{\partial r}\left(r\frac{\partial\psi}{\partial r}\right) + \frac{1}{r^2}\frac{\partial^2\psi}{\partial\phi^2} + \frac{\partial^2\psi}{\partial z^2} + k^2\psi = 0 \qquad \textit{Equation 2}$$

To solve the wave equation, a solution is required that can be separated into a radial, angular, and vertical part. The form of such a solution is given by Equation 3[50], where we define $\rho = r\sqrt{k^2 - h^2}$ and h is the separation constant.

$$\psi_n(r, \phi, z) = Z_n(\rho)e^{in\phi}e^{ihz} \quad (n = 0, \pm 1, \dots) \qquad \textit{Equation 3}$$

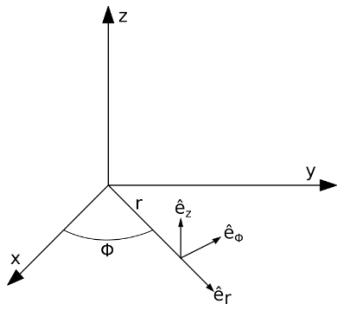

***Figure 2**. The cylindrical coordinate system used for the derivations in this chapter*

The linearly independent solutions to Z_n are the Bessel functions of the first and second kind, J_n and Y_n respectively, where n denotes their integral order. The harmonic functions for the cylinder that can be generated from Equation 3 are given as[50]

$$M_n = \nabla \times (\hat{e}_z\psi_n), \qquad N_n = \frac{\nabla \times M_n}{k} \qquad \textit{Equation 4}$$

when we take the unit vector that is parallel to the cylinder axis, $\hat{e}_z$, as pilot vector. These harmonics are then orthogonal to each other. If we now consider the interaction of a plane wave $E_i = E_0 e^{ik\hat{e}_i x}$ that is incident onto a cylinder of radius a in the direction of $\hat{e}_i = -\sin\zeta\hat{e}_x - \cos\zeta\hat{e}_z$, with ζ being the angle between cylinder axis and the incident wave, we need to express this electromagnetic wave in the cylinder harmonics that we defined above. We also need to investigate two different cases; one where electric field is parallel to the xz-plane and one where it is orthogonal to it.

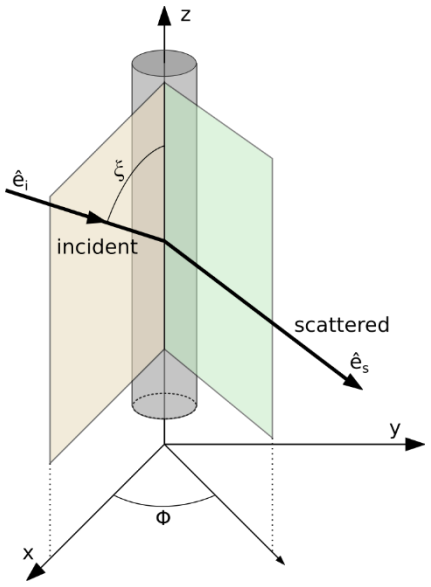

***Figure 3**. Section of the infinite cylinder used to approximate a nanofluidic channel with the Poynting vector of the incident and scattered light.*

For the first case when the electric field is parallel to the xz-plane,

$$E_i = E_0(\sin\zeta\hat{e}_z - \cos\zeta\hat{e}_x)e^{-ik(r\sin\zeta\cos\phi + z\cos\zeta)} \qquad \textit{Equation 5}$$

the expansion of this field in cylinder harmonics is given as

$$E_i = \sum_{n=-\infty}^{\infty} [A_n M_n^1 + B_n N_n^1]. \qquad \textit{Equation 6}$$

It was stated above that the Bessel functions of the second kind, Y_n, are solutions to the wave equations as well. However, at this point we must exclude them since the electric field at $r = 0$ cannot be infinite. Hence only the Bessel functions of the first kind, J_n, remain as eligible solutions. When we compare Equation 5 with Equation 3, it is also clear that the separation constant h should be $-k\cos\zeta$. Having so defined the function that generates the cylinder harmonics, $J_n(kr\sin\zeta)e^{in\phi}e^{-ikz\cos\zeta}$, we can continue following the steps in the book by Bohren and Huffman[50] to arrive at the following expressions for the coefficients A_n and B_n.

$$A_n = 0, \qquad B_n = \frac{E_0(-i)^n}{k\ \sin\zeta} \qquad \textit{Equation 7}$$

If we then define $E_n = E_0\,(-i)^n/k\sin\zeta$, the incident electromagnetic field in cylinder harmonics can now be written as

$$E_i = \sum_{n=-\infty}^{\infty} E_n N_n^1, \qquad H_i = \frac{-ik}{\omega\mu}\sum_{n=-\infty}^{\infty} E_n M_n^1. \qquad \textit{Equation 8}$$

The internal field of the cylinder in question has a similar generating function for the cylinder harmonics as the incident field, since this function is also using the Bessel functions of the first kind and needs to satisfy continuity at the boundary of the cylinder, such that $h = -k\cos\zeta$.

Here, it is now important to introduce a relation that connects to the materials inside and outside of the nanochannel. Specifically, we introduce here m, the ratio between the RI of the material that fills the cylinder ($n_{cylinder}$; in the experiments later that corresponds to a liquid or a gas) and the material the cylinder is embedded in ($n_{surrounding}$; in the experiments this will be SiO_2),

$$m = \frac{n_{cylinder}}{n_{surrounding}}. \qquad \textit{Equation 9}$$

Using this definition, the function that generates the internal field in the nanochannel is $J_n\left(kr\sqrt{m^2 - \cos^2\zeta}\right)e^{in\phi}e^{-ikz\cos\zeta}$, which is leads to the following expansions of the internal electromagnetic field

$$E_I = \sum_{n=-\infty}^{\infty} E_n[g_n M_n^1 + f_n N_n^1], \qquad H_I = \frac{-ik}{\omega\mu}\sum_{n=-\infty}^{\infty} E_n[g_n N_n^1 + f_n M_n^1]. \qquad \textit{Equation 10}$$

The scattered field assumes subsequently a similar form

$$E_s = \sum_{n=-\infty}^{\infty} E_n[b_{n1} N_n^3 + i a_{n1} M_n^3], \qquad H_s = \frac{ik}{\omega\mu}\sum_{n=-\infty}^{\infty} E_n[b_{n1} M_n^3 + i f a_{n1} N_n^3], \qquad \textit{Equation 11}$$

where the generating function $H_n(kr\sin\zeta)e^{in\phi}e^{-ikz\cos\zeta}$ is used, including the Hankel function of the first kind $H_n = J_n + iY_n$. The Bessel function of the second kind can be included here since we consider the scattered field to be an outgoing wave at large distances from the cylinder ($|\rho| \gg n^2$). Looking at the boundary conditions at $r = a$, Bohren and Huffman[50] offer the following relations for the coefficients a_n and b_n

$$a_{-n1} = -a_{n1}, \qquad b_{-n1} = -b, \qquad a_{01} = 0$$

Assuming now the common case that the incident light is normal to the cylinder axis ($\zeta = 90°$), a_{n1} vanishes and we are left with the coefficient b_n for the case of the electric field of the incident light being parallel to the xz-plane, where $x = ka$.

$$b_{n1}(\zeta = 90°) = b_n = \frac{J_n(mx)J_n'(x) - mJ_n'(mx)J_n(x)}{J_n(mx)H_n'(x) - mJ_n'(mx)H_n(mx)} \qquad \textit{Equation 12}$$

For the second case, where the incident electrical field is perpendicular to the xz-plane, the derivation for the coefficients that was laid out in Bohren and Huffman's book follows similar steps, finally arriving at an expression for a_n under the condition of normal incidence.

$$a_{n2}(\zeta = 90°) = a_n = \frac{mJ_n'(x)J_n(mx) - J_n(x)J_n'(mx)}{mJ_n(mx)H_n'(x) - J_n'(mx)H_n(x)} \qquad \textit{Equation 13}$$

We can now describe the incident, internal and scattered electromagnetic wave in terms of cylinder harmonics and have the necessary coefficients a_n and b_n available when considering the scattering from a normally incident wave of either polarization. We can therefore now calculate the scattering cross sections of our nanochannel under the approximation that it is cylinder of infinite length.

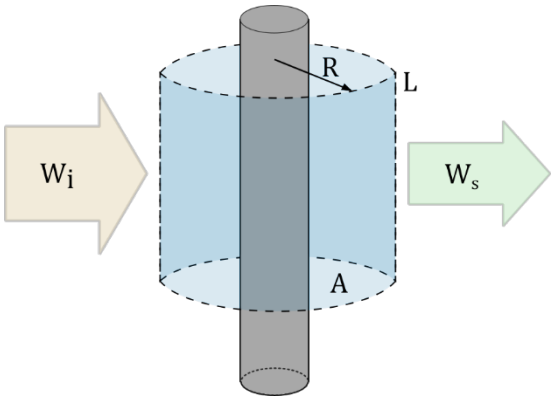

***Figure 4**. Incident light W_i and its scattered part W_s, together with the integration surface around the cylinder.*

As any infinite object would have an infinite cross section, it is advised to define the cross section with regards to a certain unit length. For this purpose, we construct a closed concentric surface around the cylindrical particle that has length L (in the direction of the z-axis) and radius R, together with a mantle surface A. This allows us to consider rates at which the incoming light is absorbed and scattered.

$$W_a = -\int_A \boldsymbol{S}\cdot\hat{\boldsymbol{n}}\, dA = W_{ext} - W_s = RL\int_0^{2\pi}(\boldsymbol{S}_{ext})_r\, d\phi - RL\int_0^{2\pi}(\boldsymbol{S}_s)_r\, d\phi \qquad \textit{Equation 14}$$

The radial components of the Poynting vector $\boldsymbol{S}$ are used above, following the definition as the cross product of the electric and magnetic field.

$$S_s = \frac{1}{2}\,\mathrm{Re}(\boldsymbol{E}_s \times \boldsymbol{H}_s^*), \qquad S_s = \frac{1}{2}\,\mathrm{Re}(\boldsymbol{E}_i \times \boldsymbol{H}_s^* + \boldsymbol{E}_s \times \boldsymbol{H}$$

Starting now with the first case that we discussed above, the incident electric field being parallel to the xz-plane, we insert the corresponding series expansions (Equation 8 and Equation 11) into the formulas above and execute the integration. This results in an expression that relates the coefficients a_n and b_n to a scattering efficiency Q_{sca}. This scattering efficiency compares the scattered radiation to the actual geometric dimension the nanochannel

$$Q_{sca,p} = \frac{W_s}{2aLI_i} = \frac{2}{x}[|b_0|^2 + 2\sum_{n=1}^{\infty}(|b_n|^2 + |a_n|^2)]. \qquad \textit{Equation 15}$$

For the second case, i.e., the electric field being orthogonal to the xz-plane, the derivation is similar and leads to the following scattering efficiency

$$Q_{sca,o} = \frac{2}{x}[|a_0|^2 + 2\sum_{n=1}^{\infty}(|a_n|^2 + |b_n|^2)]. \qquad \textit{Equation 16}$$

If the incident light is unpolarized, which is commonly the case in experiments where continuous wave light sources are used (like in my experiments), the scattering efficiency can be written as

$$Q_{sca} = \frac{1}{2}\left(Q_{sca,p} + Q_{sca,o}\right).$$

Another important simplification that we can do at this point is the assumption that we are dealing with an object that is much smaller than the wavelength of light. Specifically, if we look at x, which is defined as $x = ka = 2\pi a/\lambda$, we see that it become very small since the radius a of nanochannel I typically use in my experiments is at around 70 nm and the visible light spectrum is centered around 550 nm. This enables us to use relatively simple forms[50] of the Bessel functions needed for the coefficients a_n and b_n, that is

$$J_0(z) = 1 - \frac{z^2}{4}, \quad J_1(z) = \frac{z}{2} - \frac{z^3}{16}, \quad Y_0(z) = \frac{2}{\pi}\ln\left(\frac{z}{2}\right), \quad Y_1(z) = -\frac{2}{\pi z} \quad .$$

Inserting those expressions in Equation 11 and Equation 12 then yields the necessary coefficients for the scattering efficiencies, provided that only the terms with the smallest degree in x are considered.

$$a_o = \frac{-i\pi x^4(m^2-1)}{32}, \qquad b_o = \frac{-i\pi x^2(m^2-1)}{4}$$
$$a_1 = \frac{-i\pi x^2}{4}\left(\frac{m^2-1}{m^2+1}\right), \qquad b_1 = \frac{-i\pi x^4(m^2-1)}{32} \qquad \textit{Equation 17}$$

From here, we can go back to Equation 15 and Equation 16. Using only the terms with the highest contribution, we arrive at the following expressions for the scattering efficiencies for parallel and orthogonal incident light.

$$Q_{sca,p} = \frac{\pi^2 x^3}{8}(m^2-1)^2 = \frac{\pi^2 k^3 a^3}{8}(m^2-1)^2 \qquad \textit{Equation 18}$$

$$Q_{sca,o} = \frac{\pi^2 x^3}{4}\left(\frac{m^2-1}{m^2+1}\right)^2 = \frac{\pi^2 k^3 a^3}{4}\left(\frac{m^2-1}{m^2+1}\right)^2 \qquad \textit{Equation 19}$$

These efficiencies are given with respect to the projected surface $2aL$ that normally incident light "sees" when approaching the cylindrical nanochannel. To finally be able to write down the equations that define the nanochannel scattering cross sections, the above equations need to be multiplied by this projected surface. While doing so, the geometric nanochannel cross section, $A_\emptyset = \pi a^2$, emerges and the scattering cross sections for parallel and orthogonal polarization can be written as

$$\sigma_{sca,p} = \frac{A_\emptyset^2 k^3 L}{4}(m^2-1)^2 \qquad \textit{Equation 20}$$

$$\sigma_{sca,o} = \frac{A_\emptyset^2 k^3 L}{2}\left(\frac{m^2-1}{m^2+1}\right)^2 \qquad \textit{Equation 21}$$

If we finally assume unpolarized light irradiation, as in my experiments, we average both scattering cross section and arrive at Equation 22, which is the fundamental formula for nanochannel scattering microscopy.

$$\sigma_{sca,u} = \frac{A_\emptyset^2 k^3 L}{4}(m^2-1)^2\left(\frac{1}{2} + \frac{1}{(m^2+1)^2}\right) \qquad \textit{Equation 22}$$

Its importance is given by the fact that it combines the measured scattering intensity (through the scattering cross section) via the geometry of the fluidic system (channel dimensions) to the

properties of the medium inside the channel. We can see from this formula that a short wavelength and a large channel would in principle be beneficial for an improved scattering signal. On the other hand, in the context of measuring reaction product formed on a single catalyst nanoparticle, a large channel would lead to a more diluted product concentration in the and thus a reduced RI contrast, which consequently would reduce the sensitivity in that way. The ideal channel for NSM when used for single particle catalysis is therefore large enough to be a good scatterer but also small enough to keep the reaction products from one single nanoparticle concentrated. On a side note, it is interesting to see that if we assume a RI ratio of $m = 0.9$, the cross section for the parallel incident light contributes around 63% to the combined cross section, indicating thereby another way how the sensitivity could possibly be enhanced, i.e., by using polarized rather than unpolarized light.

2.1.2 The Kramers-Kronig relation

In the preceding section, I laid out how the scattering of light from a nanochannel depends on the difference in RI between the material inside the channel (in my case a fluid) and the material that surrounds it, and how changes in this difference induced by a catalytic rection occurring inside a channel can be detected by monitoring correspondingly induced changes in scattering intensity. However, a further interesting aspect is here that the RI in general is wave-length dependent. To this end, while liquids like pure water or transparent solids like SiO_2 exhibit refractive indices that are fairly constant across the visible spectral range, there are fluids that exhibit distinctly wavelength-dependent refractive indices, and thus also exhibit a sizable light absorption. These fluids are in most cases (aqueous) solutions of dyes, such as Pyranine, Quinoline or Coumarin, but can in principle be any compound that absorbs specific wavelengths of the visible spectrum as for example metal complexes. These absorption features lead to strongly spectrally modulated light scattering properties of a nanochannel filled with such a fluid, which in turn can be used to quantitatively analyze changes in the fluid in a spectrally resolved way.

The key to understand this effect is to understand the Kramers-Kronig relation. In a mathematical sense, this relation connects the real and imaginary part of a complex function that is analytic in the upper half plane and vanishes sufficiently fast for large arguments[51]. This complex function is the refractive index $\boldsymbol{n}(\omega) = n(\omega) + i\kappa(\omega)$, since it contains in its real part the index for diffraction and in its imaginary part the extinction coefficient. With this information at hand, we can write the Kramers-Kronig relation as[52]

$$n(\omega) - 1 = \frac{2}{\pi}\mathcal{P}\int_0^{-\infty} \frac{\omega'\kappa(\omega')}{\omega'^2 - \omega^2}\, d\omega' \qquad \textit{Equation 23}$$

where $\mathcal{P}$ denotes the Cauchy principal value of the integral. We now rewrite this equation with the use of the optical wavelength $\lambda = 2\pi c/\omega$, such that

$$\Delta n(\lambda) = n(\omega) - 1 = \frac{2}{\pi}\mathcal{P}\int_0^{-\infty} \frac{\kappa(\lambda')}{\lambda'\left(1 - \left(\frac{\lambda'}{\lambda}\right)^2\right)} d\lambda' \qquad \textit{Equation 24}$$

The relation between κ and the experimentally measurable absorption coefficient α is given by

$$\kappa(\lambda) = \frac{\alpha\,\lambda}{4\pi} \qquad \textit{Equation 25}$$

With this relation at hand, we can relate an experimentally determined absorption coefficient to the real part of the RI, as demonstrated by Sai et al[51]. In addition, and of key importance for my work, the above means that we can measure changes in the absorption coefficient of a fluid inside a nanofluidic channel in a spectrally resolved way by measuring the wavelength-dependent scattering from the nanochannel. This, in turn, opens the possibility to identify chemical compounds inside a nanofluidic channel based on their distinct spectral "fingerprint" derived from the light scattering signature of the channel. Below, in Chapter 2.3.2, I will demonstrate this concept on the example of the dye Brilliant Blue and for Allura Red in Chapter 2.4.2.

2.2 Nanofabrication of fluidic chips

Nanofluidic systems offer unique opportunities to manipulate and control fluids, both liquid and gas, at the nanoscale. Modern micro- and nanofabrication methods allow almost limitless possibilities to realize the most diverse nanofluidic designs tailored for different purposes - at least when it comes to two-dimensional architectures I used in my work. To this end, all nanofluidic systems I have used were fabricated using the facilities of the MC2 Nanofabrication Laboratory at Chalmers, which offers all the tools needed to fabricate high-end nanofluidic systems. However, while it is a true "luxury" to be able to design and nanofabricate nanofluidic devices with intricate functionalities, as I have learnt and will further outline below, it also constitutes a significant risk in terms of overengineered complexity. In fact, the most important results I have obtained used the simplest chip designs I have worked with. That said, the lessons learnt from exploring different and more complex chip designs that I discuss below have proven instrumental for both the development of NSM for single particle catalysis and the fundamental understanding of its (practical) limitations. Below, I will now provide a short summary of the key micro- and nanofabrication steps used to make such nanofluidic chips.

As a common denominator, all fluidic systems used and built for my work featured two microfluidic systems that constitute the chip in- and outlet system, which is connected to the outside world on one end and to a set of straight and parallel nanochannels on the other end (**Figure 4**). In this design, the microchannels are used to transport fluids to and from the nanochannels on the in- and outlet side, respectively. On both the inlet and outlet side, they are connected to circular reservoirs that are used for filling the fluidic system with the desired liquid. Note that in this way two different liquids can be applied on either side of the nanochannels.

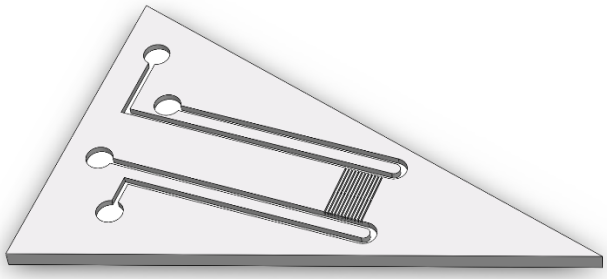

Figure 5. Rendition of a basic nanofluidic chip. Here, four inlet areas are connected via microchannels to a set of parallel straight nanochannels located at the tip of the triangular chip comprised of a thermally oxidized silicon wafer.

The micro- and nanofabrication approach used for all fluidic systems I have designed is based on so-called top-down processing into thermally oxidized silicon substrates (circular 4-inch wafers), followed by the sealing of the fluidic structures by thermally bonding glass wafers (Borofloat 33, 4 inches) onto the structured substrate. This provides both a hermetic seal and optical access to the fluidic systems from the side of the lid, which is critical for optical microscopy.

The micro- and nanofabrication process consists of the following steps:

1. Silicon wafers with (100) orientation were cleaned with a standard process. For this purpose, the wafers were first treated in SC1 (5:1:1 H_2O:NH_3OH:H_2O_2, 80°C) for 10 minutes, rinsed in deionized water, native oxide removed with 2% HF (10 seconds), rinsed again in deionized water, then treated in SC2 (5:1:1 H_2O:HCL:H_2O_2, 80°C) for 10 minutes, rinsed a final time in deionized water and then spun dry.

2. The cleaned wafers were thermally oxidized in an oxidation furnace in a water atmosphere at 1050°C. Depending on the planned application, oxide layers with a thickness of 200 nm or 2000 nm were produced. The thinner oxide layers were used when the nanochannels processed in the next step, with a typical depth of 150 nm, should have little oxide between them and the underlying silicon substrate. Accordingly, the thicker oxide layers served for cases where the distance between the nanochannels and silicon should be as large as possible.

3. In the next step, nanochannels were etched into the thermally grown oxide using reactive ion etching (RIE). For this, a 20 nm thick structured Cr layer was used as a hard mask due to its high etch resistance against the plasma used for etching the nanochannels into the oxide layer. To structure the Cr layer, a 200nm thick layer of electron beam resist (ARP6200) was prepared on top of it and the pattern of the nanochannels was defined inside that polymer layer with electron beam lithography (development in o-xylene). The pattern

created in the polymer layer was then transferred into the Cr- layer (the hard mask) with RIE using chlorine (Cl2), and the pattern in the hard mask was finally transferred into the oxide with RIE using fluorine (NF3). In the case of creating channels with vertical constrictions, the RIE of the thermal oxide was divided into two steps: (i) etching of all structures to the depth of the constrictions, and (ii) etching of all structures except the constrictions to the full depth of the nanochannels. To achieve the selective etching of the second step, protective 1 µm wide lines of photoresist (AZ5214E) were fabricated with direct laser lithography on top of the hard mask at the positions of the constrictions between the two etch steps.

4. All larger microfluidic structures were etched into the surface using RIE. For this purpose, an etching mask made of photoresist was used, which was typically structured using direct laser lithography (**Figure 6**).

5. Finally, to connect the fluidic system that now is hermetically sealed by the lid to the outer world to make it accessible for experiments, we etched holes through the silicon wafer substrate using reactive ion etching (DRIE) to provide access from the back side of the chip. In cases where a connection to the fluidic systems was used from the front side, i.e., through the glass lid, we sandblasted holes through the glass at appropriate locations.

6. For nanofluidic chips with lithographically placed nanoparticles inside the nanochannels, an additional processing step was included at this stage of the process. The nanoparticles were defined as holes with electron beam lithography (**Figure 7**) in a double layer of resist (copolymer and PMMA) spun onto the structured substrate, and the material of choice for the nanoparticles was deposited with electron beam evaporation through the holes in the resist mask. Finally, the resist mask was dissolved in acetone leaving only the nanoparticles at the defined positions on the substrate.

7. In a final processing step, the substrates were thoroughly cleaned by treating them in SC1 (5:1:1 H_2O:NH_3OH:H_2O_2, 80°C) for 10min followed by a rinsing step in DI water and blow drying with N_2. Glass wafers of 175 µm thickness were cleaned in the same manner, O_2-plasma treated (50W RF power, 250 mTorr) together with the processed substrates and thermally bonded to the substrates at 550°C for 5hrs prior to dicing them into individual fluidic chips used for the catalysis experiments.

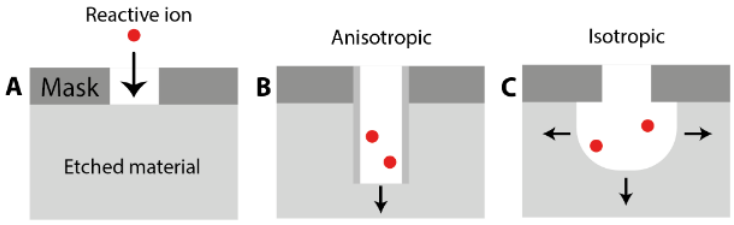

***Figure 6**. Reactive ion etching (RIE). a) A reactive ion (fluorine for SiO_2 etching, oxygen for polymers) is accelerated in an electric field towards the substrate, knocking out atoms from the surface and/or chemically reacting and forming volatile compounds that then detach from the surface. Thereby RIE removes material from areas where the substrate is not protected by the mask. b) Anisotropic etching can be achieved by tuning the ratio of physical and chemical etching or by protecting the side walls with a polymer in cycled steps between the etching. c) Isotropic etching of the substrate is achieved by leaving the side walls unprotected and tuning the etching parameters. Adapted work*[53].

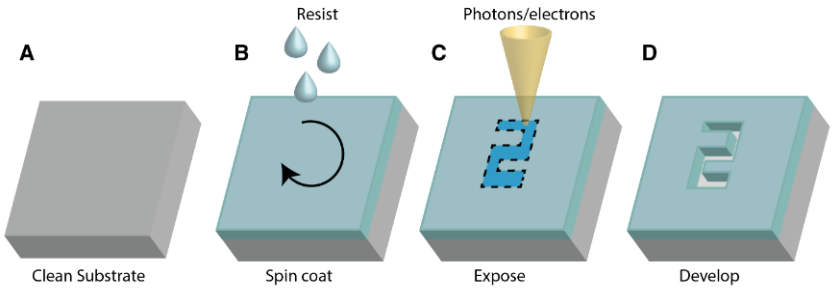

***Figure 7.** Nanolithography. A clean substrate (a) is spin coated with a polymer-based resist that is sensitive to exposure to electrons or photons (b). c) Exposing the resist to light or electrons alters its structure, e.g., through cross-linking or splitting of polymer chains, such that it becomes (in)soluble in specific solvents and can be removed in the exposed areas during the development step (c). Adapted work*[53].

2.3 The microscope setup and first results

2.3.1 The setup

For my experiments, I used dark-field scattering microscopy where the name stems from the illumination scheme. In contrast to bright-field microscopy, where the light that is transmitted through the sample or reflected from it, we monitor here only light that is scattered from the sample. For this, a special objective with high numerical aperture is needed that illuminates the sample surface at a shallow angle and at the same time only collects scattered light (**Figure 8**).

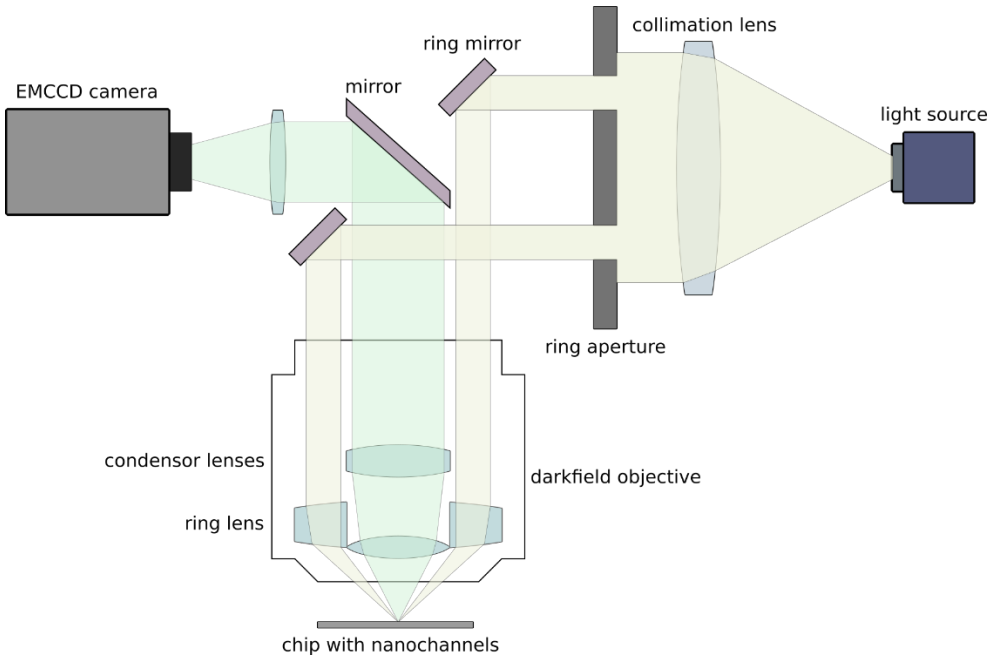

***Figure 8**. Schematic of the darkfield microscopy setup used for the nanofluidic scattering microscopy experiments.*

For the work presented in this thesis, I used three different microscopes with different characteristics, light sources and cameras. However, their principle of operation was the same in the sense that they all were operated in dark field scattering mode. Below, I will describe the setup I used in the early phase of my project, together with correspondingly obtained results.

This first setup was comprised of an upright Nikon Eclipse LV 1000 microscope equipped with a Nikon TU Plan ELWD 50x/0.60B darkfield objective and a Märzhäuser Wetzlar Tango 3 Desktop electronic microscope stage. For illumination, I used a Nikon LV-LH50PC halogen lamp, which produces a relatively even spectrum across the visible regime (**Figure 10**). The scattered light collected by the darkfield objective was directed into a Andor Shamrock SR-303i-B spectrometer before being recorded by a Andor Newton DU920P-BR-DD CCD camera. If not used in spectroscopic mode, that is to measure scattering intensity as a function of wavelength, the 150 l/mm grating of the spectrometer can be adjusted such that the 0^{th} maximum reproduces the microscope image onto the CCD camera, thereby enabling operation of the setup in imaging, rather than spectroscopy, mode. This enables the imaging of a large number of nanochannels in parallel (as I did later in this thesis, see **Figure 28**). In contrast, when operated in spectroscopy mode, only a single channel can be analyzed since the image of the channel has to be aligned with the entrance slit of the spectrometer.

To start an experiment, I introduced the necessary liquid(s) to the system by filling reservoirs in the chuck that host the fluidic chip and that connect to the reservoirs in the chip at the end of the microfluidic systems of (**Figure 9**). Once filled with liquid, by applying pressure (typically 2 bar) to these reservoirs via a system of pressure pipes, I then control the direction of liquid flow through the chip, as well as the flow rate. To exchange the liquid(s) in the system, the chuck was opened, the present liquid extracted from the reservoirs with a syringe and the new liquid was filled in.

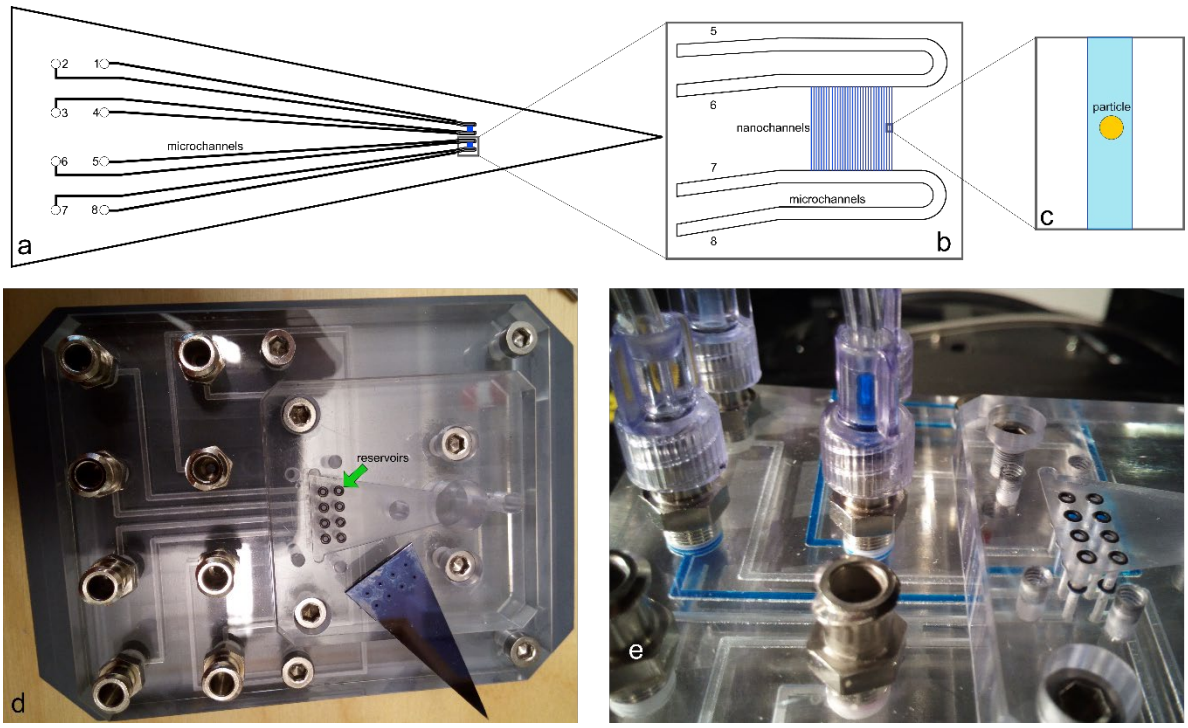

***Figure 9**. a)-c) Schematic of the fluidic design of my first chips with the microchannels in black, the nanochannels in blue and the position of a single nanoparticle in yellow. d) The chip holder, also referred to as chuck, with the fluidic chip mounted on top. The chip is shown from its inlet (holes) side. c) Detail of the chuck, where two inlet channels have been filled with Brilliant Blue solution for highlighting the pathway of the liquid into the chip. The attached pipes lead to the pressure source used to control the flow through the chip.*

2.3.2 Wavelength-resolved scattering intensity measurements of transparent liquids

As laid out in chapter 2.1.1, the light scattering properties of a nanochannel are defined by its geometry and by the ratio of the refractive indices of the material surrounding the channel (SiO_2) and the liquid inside the channel. To verify the corresponding theory I have presented above in a first experiment using transparent liquids with different RI, I measured the spectrally resolved scattering intensity of light from a single nanochannel filled with pure Milli-Q water and of the same channel filled with a 30 % aqueous H_2O_2 solution (**Figure 10**). The procedure for these first measurements was as follows: All 4 reservoirs for one side of the chip in the upper transparent part of the chuck were filled with water, and the chip screwed on top with the inlet holes pointing down. 2 bar pressure was applied to two of the reservoirs so that the water was pressed in via the holes into the microchannels and established a flow through them. After several minutes in this state, the pressure from one of the inlet holes was lifted, such that one microchannel now had an overpressure of 1 bar at the entrance to the nanochannels with respect to the microchannel at the other side of the nanochannels. This pressure difference across the nanochannels then initiated a flow through them and enabled their complete filing with water after several minutes. While the chip was being flushed with water in this way, the

chuck was placed under the microscope, with the nanochannel area positioned in the center of the field of view of the camera. From the 340 µm overall length of the nanochannels, 170 µm fit the field of view. Notably, it is important to not include the connection of the nanofluidic system to the microchannels in the field of view to avoid background scattering form the microchannel walls. To measure scattering spectra from a single nanochannel, I closed the entrance slit of the spectrometer such that only the scattering signal from a single nanochannel is recorded. By then setting the center wavelength of the grating to 641 nm, spectrally resolved scattering intensity can be measured along the nanochannel aligned with the slit of the spectrometer. Typically, for such a measurement I accumulated 10 frames with 0.5 s exposure time per frame and took the average. To further reduce readout noise and minimize the amount of data, the whole spectrum was binned along the nanochannel in the camera if no spatially resolved spectroscopic measurement was required.

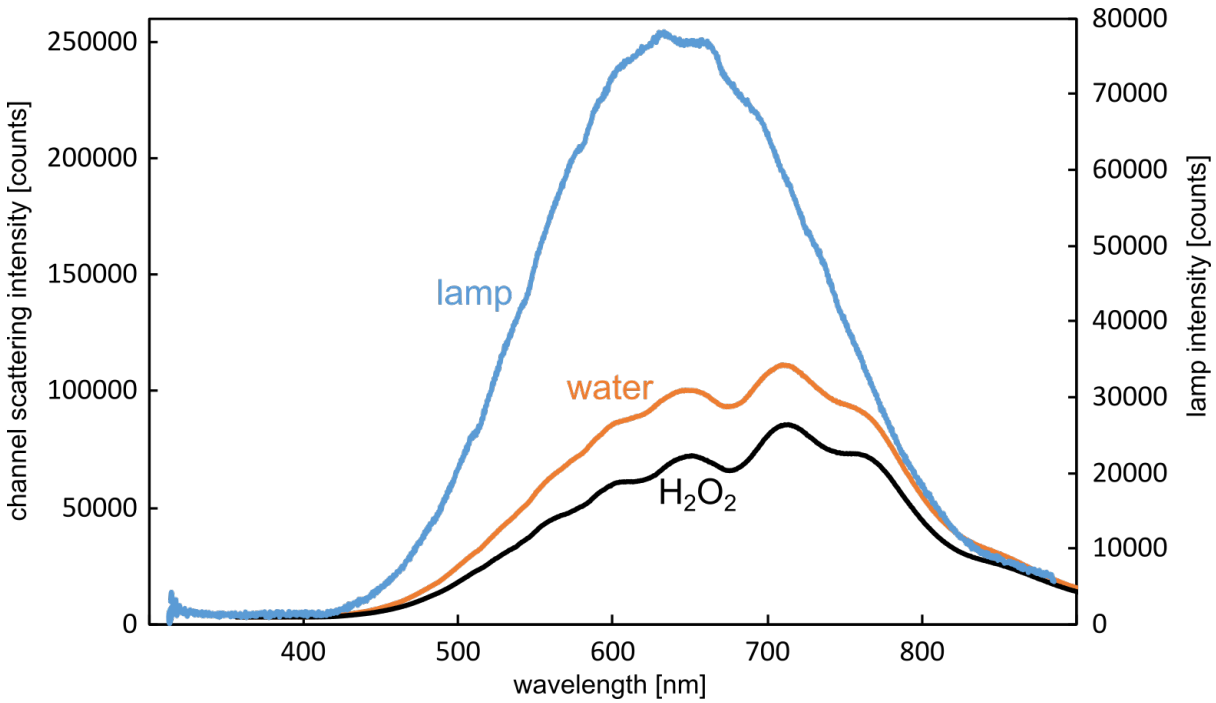

Figure 10. *Emission spectrum of the halogen lamp (blue) used for sample illumination obtained by measuring the light scattered from a reflectance standard, together with the spectrally resolved raw and unreferenced light scattering intensities from a single water-filled nanochannel (orange) and the same channel subsequently filled with a 30 % aqueous H_2O_2 solution (black). The lamp spectrum is drawn on the secondary y-axis as the acquisition settings were different.*

Analyzing the correspondingly obtained scattering spectra in **Figure 10** reveals a Gaussian intensity distribution for the lamp spectrum, with small features at the peak, which is expected for a halogen lamp[54]. In comparison, both scattering spectra from the nanochannels still show an intensity distribution that is close to a bell shape, but they are also clearly deformed and show additional features. The origin of these changes is not found in the optical path between chip and camera, as the lamp spectrum was recorded the same way, but it lies within the

scattering properties of the fluidic chip itself. Water[55] and H_2O_2[56] show significant absorption only above 700 nm and below 300 nm, which means that they can be regarded as fully transparent in the wavelength range we discuss here. Hence, the most remarkable observation that we make in this experiment is the overall scattering intensity difference measured for the channel filled with water and 30 % aqueous H_2O_2 solution, respectively. The explanation for this observation is indeed the RI difference between the two liquids, as outlined in detail below.

The key result of the theoretical derivation in chapter 2.1.1 was Equation 22, which connected the scattering cross section of a nanochannel to the RI difference between the medium inside and outside of the channel. I will now use this equation to plot the theoretical scattering cross section for a 140 nm x 140 nm nanochannel of 170 µm length that is illuminated by 550 nm light (**Figure 11**.). To show the general behavior of this function, the RI range for the medium inside the channel is varied from 0.8 refractive index units (RIU) to 2.4 RIU.

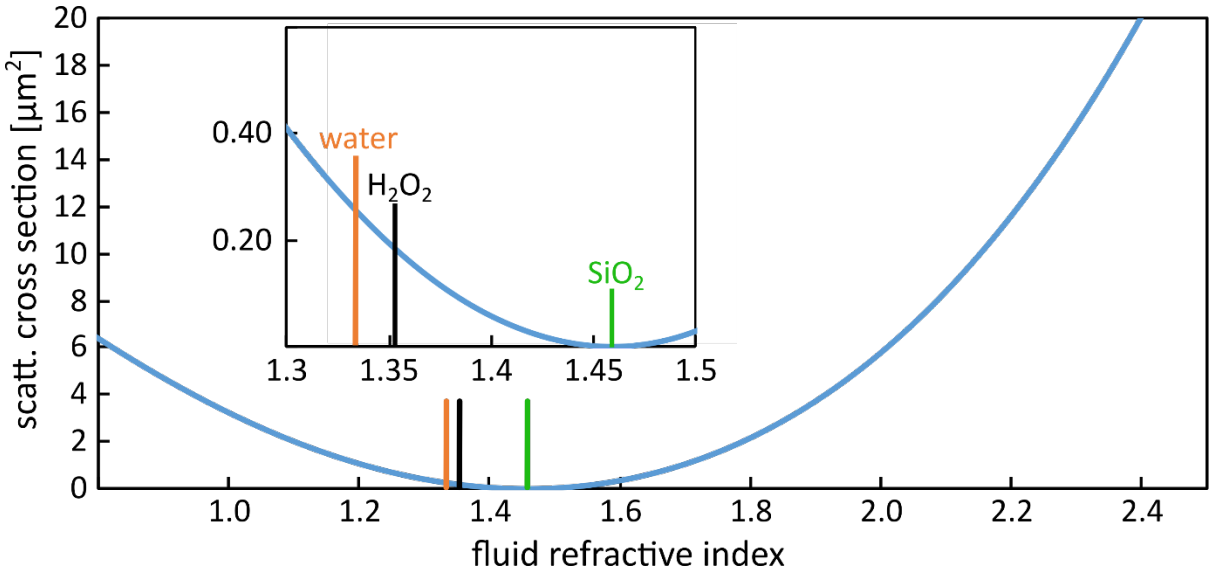

***Figure 12**. Theoretical scattering cross section (blue) of a 140 nm x 140 nm nanochannel of 170 µm length calculated using equation 22 and plotted over a wide range of refractive indexes for the medium inside the channel. The markers indicate the refractive indexes for SiO_2 (1.4585 RIU), water (1.3333 RIU) and a 30% aqueous H_2O_2 solution (1.3529 RIU).*

The RI dependence of the calculated nanochannel scattering cross section exhibits a minimum at exactly the RI value of SiO_2 (1.4585 RIU)[57]. The explanation can be found by analyzing Equation 22 or by considering that a channel filled with SiO_2 while being also embedded in SiO_2 would be optically invisible since no light could scatter from it. Hence, its scattering cross section (SCS) is zero. When the channel is filled with water (1.3333 RIU)[58], however, we see that the SCS of the channel is now approx. 0.28 µm^2. This means that the channel will now scatter light efficiently and will become visible in an experiment such as the one summarized in Figure 10. Exchanging now the liquid in the channel from pure water to an aqueous 30% H_2O_2 solution, we also change the RI to 1.3529 RIU[59] which according to equation 22 yields a SCS of 0.19 µm^2, which is significantly lower that for the water filled channel (see also inset in **Figure 13**.). This is the explanation for the result that we see in the measurement shown in **Figure 10**, where indeed the scattering intensity of the water filled nanochannel is higher than for the H_2O_2 filled one.

2.3.3 NSS of a Brilliant Blue solution

Having experimentally corroborated the theoretical background of NSM introduced in chapter 2.1.1 for measuring RI induced changes in light scattering intensity of a single nanochannel filled with different *transparent* liquids in chapter 2.3.1, it is now interesting to perform similar experiments with a liquid that *absorbs light* in the visible range to show the connection between experiment and the theoretical prediction by the Kramers-Kronig relation (Equation 24).

Specifically, I used for this test the (former) food dye Brilliant Blue, due to its non-toxicity and strong absorption in the visible, and a nanofluidic system comprised of nanochannels with the same dimensions as for the test with the transparent H_2O_2. The experimental procedure is identical to the one described above, with the exception that now I filled one reservoir of the inlet microchannel with water while the other reservoir of the same microchannel was filled with the Brilliant Blue dye solution. By doing so, I could now exchange the liquid in front of the nanochannels by switching the pressure from one reservoir to the other, without having to remove the fluidic chip from the microscope. The solution that I used had a concentration of 50 mM Brilliant Blue in water and was prepared by dissolving solid dye powder in ultrapure MilliQ water.

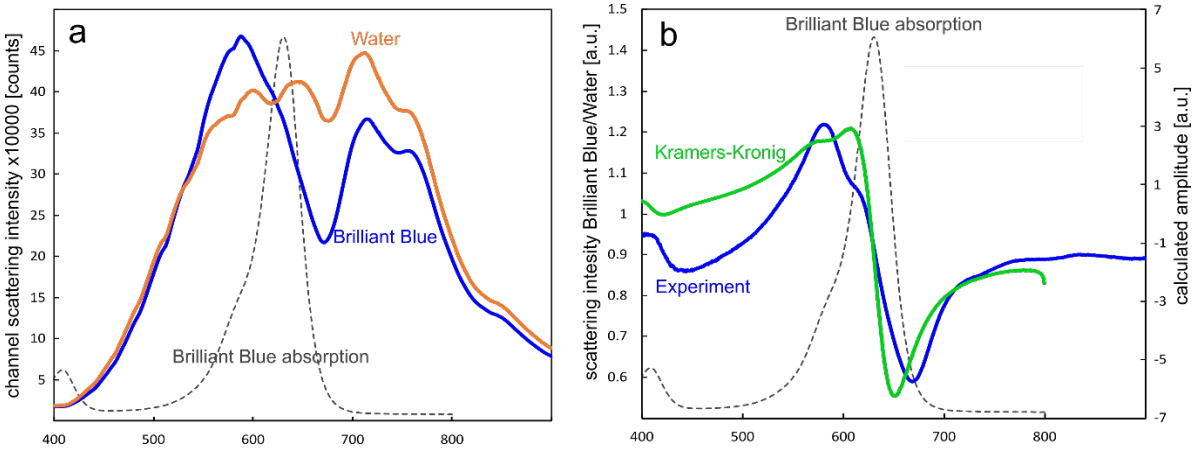

***Figure 14**. a) Experimentally measured scattering spectra of a single nanochannel filled with pure water (orange line) that was subsequently replaced by a 50 mM Brilliant blue solution (blue line). Also shown is the absorption spectrum of Brilliant Blue[60] (dashed black line). b) Dividing the spectrum of the dye-filled channel filled by the spectrum of the water filled channel yields the referenced experimental scattering spectrum for the Brilliant Blue dye (blue line). It is plotted together with the RI spectrum (green line) calculated using the Kramers-Kronig relation (Equation 24) with the absorption spectrum (black dashed line) as input.*

The impact of the dye solution on the scattering intensity spectrum of a single nanochannel is clearly visible already in the raw spectrum (**Figure 14a**). Specifically, we see a drastic reduction of the scattering around 670 nm, while the scattering is enhanced around 587 nm when comparing to a water-filled channel. This is, at first, a somewhat puzzling result since if it only were light absorption of the dye that is seen in the spectrum, we would only expect a reduction of the scattering intensity and not an increase as we see around 587 nm. It is also curios that these distinct peaks appear in wavelength ranges where the absorption of the dye increases or decreases, respectively.

To understand this, we remind ourselves that the origin of the measured scattering intensity spectrum is to be found in Equation 22, where that SCS depends on the refractive index of the medium inside the channel. Knowing the Kramers-Kronig relation (**Equation 24**), we know that the refractive index of a medium can be wavelength dependent and is connected to its absorption spectrum. When we now want to know how the refractive index changes with the wavelength, we need to insert the absorption spectrum of our dye Brilliant Blue (shown in **Figure 14**) into the Kramers-Kronig relation and perform a numerical integration. The resulting refractive index spectrum is shown in **Figure 14b**. Also plotted is the scattering spectrum of the nanochannel with the Brilliant Blue solution, which has been divided by the scattering spectrum of the water filled channel to show only the features that stem from the dye itself.

It is evident that the theoretical spectrum calculated using the Kramers-Kronig relation, and the experimentally measured spectrum have a very similar shape. More specifically, the peaks at 586 nm are very similar in both curves and the shoulder seen at 612 nm in the experimental curve corresponds to the peak in the theoretical spectrum at the same position. Similarly, the (negative) peaks at 660 nm are close for both curves, even though their position differs slightly. In summary, from this analysis it becomes clear that those distinct peaks appear in the refractive index spectrum at positions where the absorption spectrum changes rapidly. This opens the door to using NSM to specifically identify chemical compounds (formed) inside a nanochannel during a catalytic reaction via the scattering spectrum. Hence, it essentially establishes widely used optical absorption spectroscopy inside nanofluidic channels on tiny liquid volumes, which constitutes a significant step beyond the state of the art.

Concluding these first two experiments with both a transparent and light absorbing liquid in a single nanochannel, I want to highlight that wavelength resolved NSM, which we from here on forward call Nanofluidic Scattering Spectroscopy (NSS), indeed enables the characterization of a liquid inside a single nanofluidic channel based on its RI, in good agreement with the corresponding theoretical predictions. On the other hand, if a solution that is transparent in the visible regime is to be investigated, monitoring a scattering intensity change is most convenient and proportional to the RI of the liquid in the channel (Equation 22). For liquids that have an absorption band in the wavelength range of interest, in addition to monitoring scattering intensity changes proportional to concentration in NSM, we can use the spectral resolution provided by NSS to quantitatively extract absorption spectra of the liquid inside a single nanochannel using the Kramer-Kronig relations. Thereby it becomes possible to obtain a spectral fingerprint of the composition of the liquid inside the channel and potentially monitor changes in this composition in a quantitative way.

2.4 Setup and nanofluidic chip refinement towards single particle catalysis

2.4.1 First stage of refinements

This first stage in the refinement of NSM and NSS towards single particle catalysis applications included several changes and improvements of the microscope setup itself, the chuck holding the chips, the nanofluidic chip design and data treatment and evaluation.

On the microscope side, I started to use a Nikon Eclipse LV1500N upright microscope equipped with a Nikon TU Plan ELWD 50x/0.60B darkfield objective and a Prior H101P2NLV/A electronic microscope stage. As the key difference, this setup features an Andor Newton DU920P-BEX2-DD CCD camera with higher sensitivity towards shorter wavelengths of the visible spectrum. The second main difference is to be found in the Andor Shamrock SR-193I-A-SiL spectrometer onto which the camera is mounted, since it is in addition to the 150 l/mm diffraction grating also is equipped with a mirror that enables efficient imaging of nanofluidic samples since it ensures a higher photon throughput to the camera. Finally, since the scattered light intensity measured is proportional to the incident light intensity, I also exchanged the halogen lamp used for sample illumination in my first experiments to a Thorlabs Solis 3C LED lamp with a 4 W power output. This, in turn roughly doubled the scattering intensity from a single channel and enabled a higher time resolution in my experiments, as the exposure time to saturate the camera can be shortened. Furthermore, it features a very short stabilization time and essentially zero intensity drift over time, such that the output power can be regulated without waiting time and all frames of a time series are comparable to each other.

A further significant hardware improvement was a Fluidgent MFCS-EX-5C multichannel pressure controller that allows the accurate electronic control of the pressure applied to up to 8 separate channels in the range from 2 mbar to 7 bar. In this way, it enables the very accurate control of the liquid flow through my chips across a wide range and in a more reproducible way than the manual pressure controller I used for the first series of experiments. An additional key aspect of this device is that it enabled me to control electronically all key components of the experimental setup, i.e., the microscope stage, the spectrometer, the camera, and the flow control system. Consequently, it became possible to fully automatize my measurements, as I describe in detail further below in chapter 2.4.2.2. This constitutes an important advance because we aimed to measure more channels simultaneously in a consistent manner and because it enables more effective use of working time.

To improve the flexibility of my experiments in terms of using more sophisticated and intricate nanofluidic chip designs, such as the inclusion of reference nanochannels I will discuss in detail below, we also designed a new chuck that is able to host an entire 4-inch wafer (rather than just a triangular slice of it as shown in **Figure 1** and **Figure 9**). It therefore provides more space on the chip for complex fluidic designs (**Figure 15**). This chuck featured 8 liquid inlet connections equipped with glass tubes for compatibility both with organic solvents and other chemically harsh liquids (the glass tubes can be seen in **Figure 20a** in the transparent perimeter of the chuck.

Concerning the new chip design, it included the following key points:

(i) The addition of different arrangements of Au catalyst nanoparticles inside the nanofluidic channels at a predefined position using electron beam lithography (**Figure 7**). These nanoparticles all had a thickness of 20 nm, a diameter of 50 nm and were placed in parallel nanochannels in different numbers, that is, 1, 5, 10, 100 and 200 particles per channel. In addition, we also decorated nanochannels with nanoparticles with 100 nm diameter and in the same numbers as the 50 nm particles.

(ii) The implementation of colinear empty (i.e., without particles) reference nanochannels with dead ends placed above and below to the reaction channels with the particles (**Figure 15b/c**). These reference channels serve the purpose to remain filled with a reference liquid (water for the work presented in this thesis) during the entire experiment while in the particle-filled channels the liquid/reactants are exchanged. In this way, simultaneously measuring the optical response from the reference channels and the channels in which the catalytic reaction occurs, enables the continuous optical referencing of the reaction channels (**Figure 15c**). This is expected to eliminate intensity fluctuations and drifts from the light source, as well as effects from slow microscope defocusing and background scattering from the measured signal.

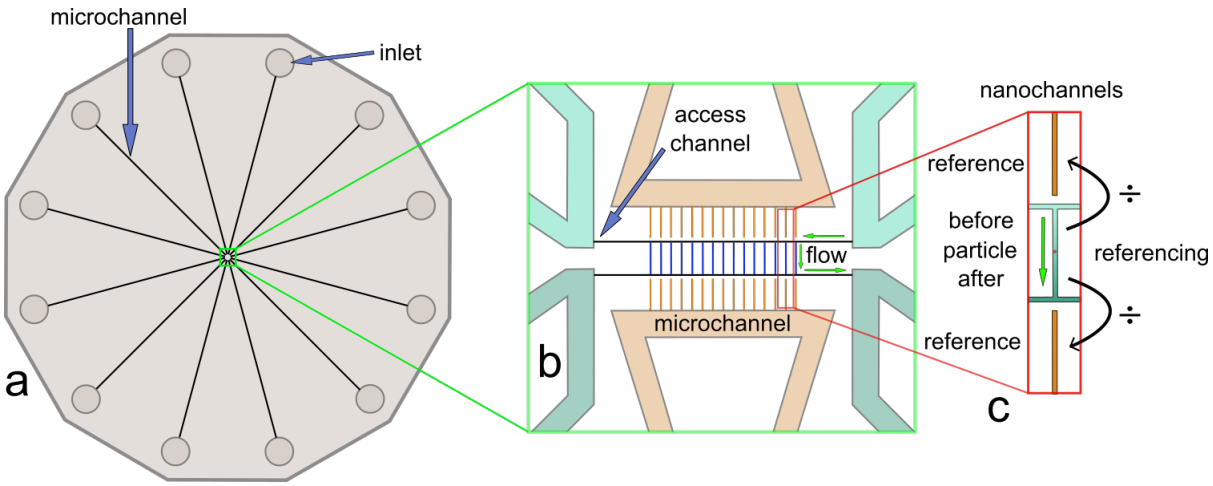

***Figure 15**. Schematics of the new fluidic chip design. a) The fluidic chip was fabricated from a 4-inch silicon wafer. Inlets are positioned on the outer border of the wafer with microchannels connecting them to the nanochannels in the middle. b) Nanochannel area, showing the nanochannels containing the particles in the middle (blue) and the isolated reference channels (orange). Flow of reagents into the nanochannels is established via the access channels that are connected to the microchannels leading to the inlet reservoirs. c) Enlarged nanochannel arrangement showing the isolated reference channels that are colinear with the nanochannel containing the particle(s) and localized both above and below the reaction nanochannels. In this way, the reaction channels and the reference channels could be placed in the slit of the spectrometer and recorded spectrally at the same time.*

At the global level, even with these new features, the basic fluidic system design used was retained and featured microfluidic in- and outlet systems as before that connected to the nanofluidic system comprised of parallel nanochannels that this time either are empty (dead end reference channels) or decorated with a specific number of nanoparticles (reaction

channels). As the main difference, the inlet reservoirs are now arranged in a circular fashion around the entire wafer (see also **Figure 20a**) and the chip features two separate fluidic systems that can be filled and controlled independently: (i) the reaction system with parallel nanochannels featuring the Au particle arrangements and (ii) the reference system with the empty nanochannels (**Figure 15**).

To then prepare an NSS measurement of a reaction in a single nanochannel, the entire fluidic system of the chip, that is, both reference and reaction systems, were filled with water to measure a scattering spectrum of all channels and channel regions of interest: (i) the upper reference channel, (ii) the section of the reaction channel upstream of the particle, (iii) the section of the reaction channel downstream of the particle, (iv) the lower reference channel. When subsequently comparing the scattering spectrum taken from the reaction channel upstream of the particle with the upper reference channel spectrum (and likewise for the downstream fraction of the reaction channel and the lower reference channel) as shown in **Figure 15c**, we obtain the intrinsic difference in light scattered from the selected fraction of the reaction channel and the corresponding reference channel. In this way, during a catalysis experiment in the reaction channel, we can subtract all non-reaction related contributions to the measured scattering spectra by subtracting the simultaneously measured scattering response from the scattering channels adjacent to the up- and downstream fractions of the reaction channel, thereby hopefully increasing the resolution of our system.

With this upgraded microscope setup and the new chip design at hand, I took the step to for the first time attempting the study of a catalytic reaction on the Au nanoparticle arrangements inside my nanochannels. As the model reaction, I used the catalytic degradation of the azo-dye Allura Red with the strong reductant sodium borohydride ($NaBH_4$). Allura Red has a distinct absorption band in the 500 nm wavelength region (**Figure 16a**), such that I expect a broad peak in the scattering spectrum between 500 nm and 600 nm when flushing the solution in the nanochannels[60].

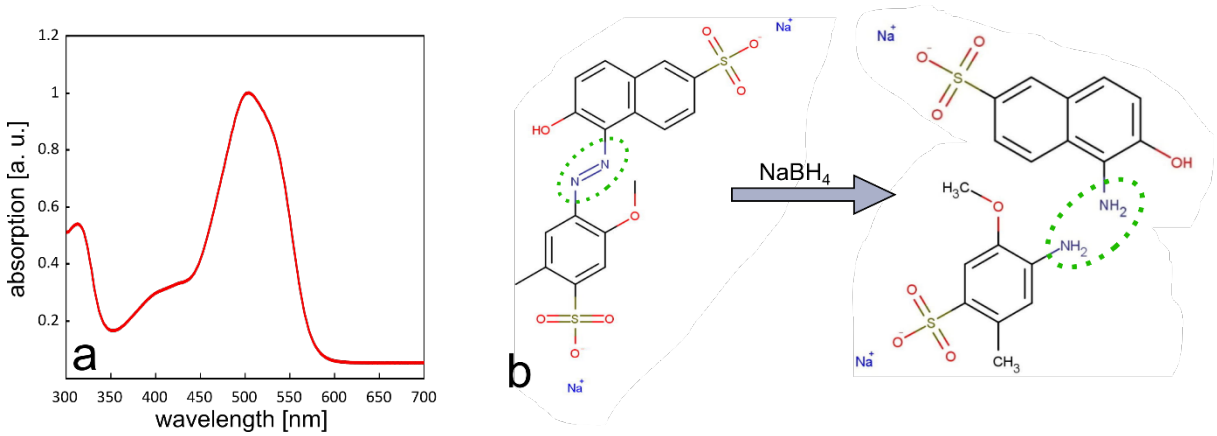

***Figure 16**. a) Normalized optical absorption spectrum of the Allura Red dye. b) Catalytic decomposition of Allura Red with $NaBH_4$ into 2-methoxy-5-methyl-aniline-4-sulfonic acid and 1-amino-2-naphthol-6-sulfonic acid on an Au catalyst[61] (structures adapted from same source).*

Allura Red decomposition is a reaction that, for example, has been investigated for sewage treatment purposes since dyes of the azo group are known to be toxic and carcinogenic in large quantities and persist for a long time in the environment[61–66]. Mechanistically, the

decomposition of Allura Red can be done via oxidation[62,64] or by reduction[61]. In both cases, it is the name-giving nitrogen double bond (French *azote* = nitrogen) in the center of the molecule that is broken during the reaction according to the following mechanism. The reaction pathway mediated by $NaBH_4$ on Au (**Figure 16b**), starts with the organic dye that is adsorbed onto the gold surface, as it known for other organic dyes such as nitrophenol[63,66,67]. Simultaneously, also the borohydride molecules adsorb on the Au surface and dissociate into hydrogen and hydroborate that goes back into solution[66]. As described for similar reactants[61], the hydrogen from the borohydride will activate the nitrogen double bond in the dye and form NH_2 groups. In this way the double bond is broken and the dye molecule breaks into two organic acids that are colorless an desorb from the Au surface back into in solution[61].

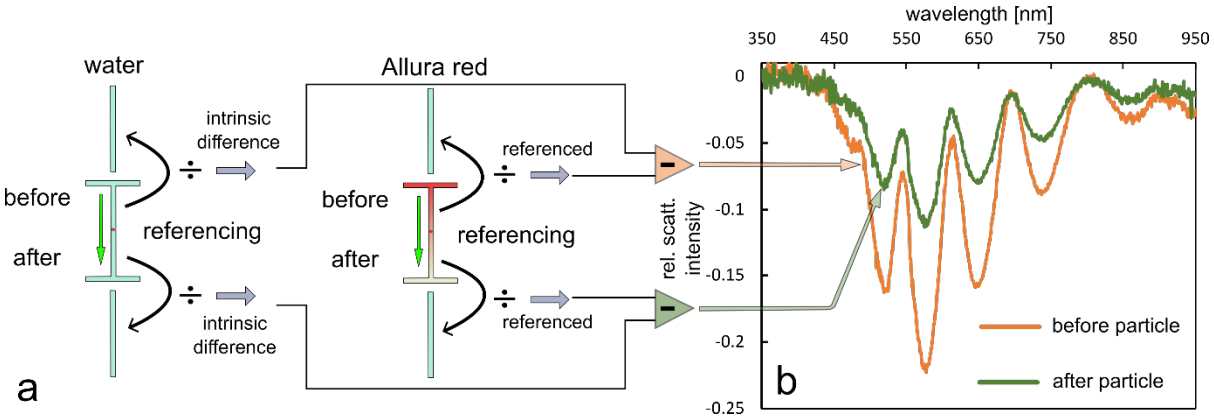

***Figure 17**. a) Evaluation scheme for fluidic systems with reference channels during catalytic Allura red decomposition on Au nanoparticles inside the nanochannels. b) Nanochannel scattering spectra obtained according to the scheme in a) for the decomposition of a 100 mM Allura Red solution by 200 mM $NaBH_4$ on a 100 nm wide and 200 nm long gold nanoparticle inside a single nanochannel. The spectra were measured upstream of the particle (orange) and downstream of it (green). The pressure applied at the inlets with Allura Red was 2 bar. Note the distinct difference between the two spectra, as well as the interference-type modulation of the signal in both of them.*

In view of this reaction mechanism and the colorless product molecules formed, it is clear that this reaction creates a distinct optical contrast and is therefore a perfect test system for the NSS concept in a scenario where this optical contrast is produced within the nanochannel, at the position of the catalyst nanoparticle by the decomposition reaction. Specifically, to define and measure this optical contrast induced by Allura Red decomposition on the Au nanoparticles inside the nanofluidic chip introduced in **Figure 15**, I used the evaluation scheme depicted in **Figure 17a** based on the on-chip referencing scheme introduced above.

As the main result, we observe a distinct difference in the referenced scattering spectra measured up- and downstream of the particle (**Figure 17b**), with the overall intensity difference (compared to water) decreasing (less negative) after the particle. This is in good agreement with a significant fraction of the dye molecules having been decomposed, therefore rendering the solution more transparent and water-like. On one hand, this was a very encouraging result in the sense that it (i) nicely corroborated my key intentions with this fluidic system, that is, a very stable baseline owing to the continuous referencing with the water-filled reference channels, and (ii) proved that the catalytic reaction is measurable via a change in the scattering spectrum of the nanochannel. On the other hand, it also was disappointing because the spectra

shown in **Figure 17b** are heavily modulated by what appears to be an interference pattern. This masks any distinctive features of the RI spectrum of Allura Red and thus renders any more quantitative analysis of the obtained spectra and their evolution over time essentially impossible. I will discuss the interference problem in more detail in chapter 2.4.2.1.

Despite these interference issues, as a further proof of concept, I executed a second set of experiments using the same fluidic system and the dye Brilliant Blue to further investigate the performance of the on-chip referencing scheme (**Figure 18b**). Note, however, that no catalytic reaction takes place in this case. Instead, to create different optical contrast in the channel, I prepared a series of aqueous Brilliant Blue solutions with 100 mM, 75 mM, 50 mM, 25 mM and 10 mM concentrations, respectively, and flushed them subsequently through the channels to systematically monitor the nanochannel scattering response as a function of dye concentration.

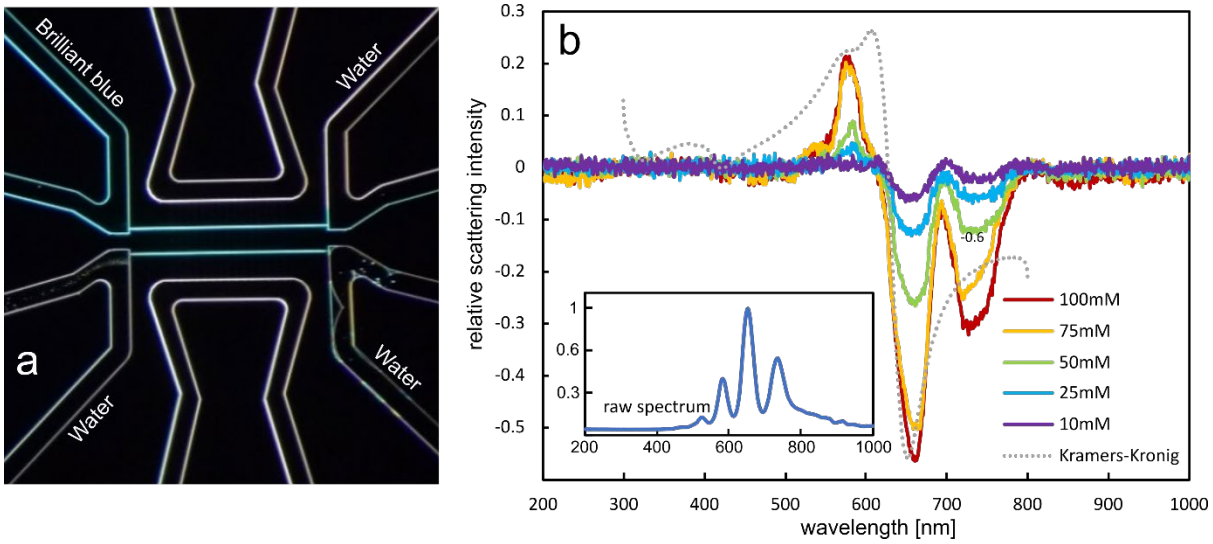

***Figure 18**. a) Dark-field micrograph of the central nanochannel section, where Brilliant Blue is flushed in from the upper left microchannel. A slight blue hue can be seen from the walls of the microchannel as well as from the access channels leading to the nanochannels, which are too dark to see in this picture. d) Referenced scattering spectra of one nanochannel for a concentration series of Brilliant Blue, together with the theoretical RI spectrum as shown in **Figure 14b**. The inset shows the unreferenced raw scattering spectrum from one of the nanochannel sections adjacent to the nanoparticles.*

Looking at **Figure 18b** that depicts referenced scattering spectra for different Brilliant Blue concentrations, the positive effect of the referencing to the water filled reference channels manifests itself in the very flat baseline that shows no offset for any of the measurements. This again corroborates that the reference channels function as intended and significantly improve the obtained scattering spectra from the dye-filled nanochannel. The dependency of the scattering spectrum intensity on the concentration of Brilliant Blue in the solution is also clearly visible as the distinct features diminish with lower concentrations and already here hints at the linear dependence of the scattering intensity on the RI (and thus concentration) of the liquid in the channel that we in detail investigated in the manuscript appended to this thesis.

When comparing the Brilliant Blue scattering spectra that I measured from the nanochannel with the theoretical RI spectrum calculated before, using the Kramers-Kronig relation (**Figure 18b**), we see that the overall similarity is still there, together with some key features. However,

also here the spectra are heavily modulated by interference. This becomes even more apparent when considering how a raw spectrum, prior to referencing, looks like (see inset in **Figure 18b**). At the same time, even if some of the modulation remains, it again demonstrates the value of the on-chip referencing concept since the modulation is substantially reduced. The main reason why it is not eliminated completely is that interference is extremely sensitive to local variations on the chip and varies therefore across different locations on the chip. I will address the origin of this problem in detail below in chapter 2.4.2.1.

2.4.2 Second Stage of refinements

The results that I have obtained so far from the improved experimental setup were encouraging and proved that the made modifications contributed greatly to the overall performance of the NSM and NSS approach. In addition, I was able to show that we indeed can monitor a catalytic reaction on a single particle with a nonfluorescent compound. Unfortunately, however, the interference modulation of the spectra made further quantification of the obtained results impossible and also preclude further use the nanofluidic chips. Accordingly, to resolve the problem in a second stage of refinements, I start out by investigating the origin of the interference patterns in the scattering spectra.

2.4.2.1 Eliminating interference

Looking at the spectra shown in **Figure 17b and Figure 18b**, the fringe pattern appears quite regular and the width of the interference peaks increased slightly for longer wavelengths. This sparked the idea that I was dealing with a basic physical phenomenon. After some investigation, it became apparent that this indeed was the case since the fringe pattern visible in the scattering spectra is the result of thin film interference. More specifically, the interference is generated when the incident light is reflected not only from the surface of the oxide into which the nanochannels are fabricated, but also from the surface of the silicon under the oxide, as depicted in **Figure 19b**. To corroborate this hypothesis, I calculated this interference following Gungor et. al.[68], using 3.88 as the RI of silicon[69] and neglecting its extinction. The result can be seen in **Figure 19c**, where I used 2 µm as the nominal thickness of the oxide that is on the silicon wafer and in which the nanofluidic system is embedded. This theoretically obtained fringe pattern matches quite well with the experimental data, even though the peaks match not exactly since the actual oxide thickness on my sample might be slightly different from the targeted 2 µm. That the calculation yields the same number of interference peaks within the spectral range of the light source and that the peak width increases for longer wavelengths further corroborates my assumption that thin film interference distorts the scattering spectra of the nanochannels in the current chip design, due to the unfortunate choice of a 2 µm thick oxide layer on the silicon wafers used for the fabrication of the chip.

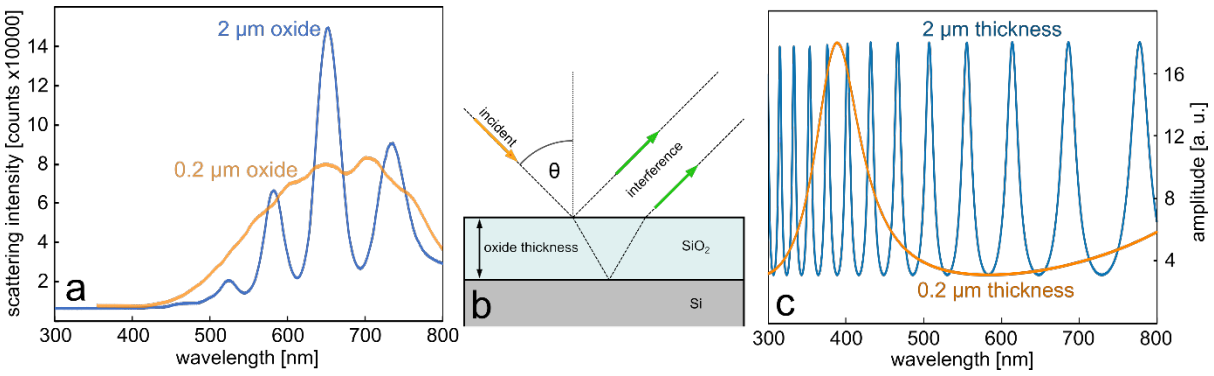

***Figure 19**. a) Nanochannel scattering spectra for a water-filled nanochannel etched into 2 µm thick SiO_2 (blue line) and etched into 0.2 µm SiO_2 (orange line). In both cases the typical interference fringe pattern can be seen. However, it is dramatically reduced when 0.2 µm SiO_2 is used to host the nanochannel. b) Schematic depiction of the principle of thin film interference. c) Calculated fringe patterns for SiO_2 layers of 2 µm and 200 nm thickness.*

To amend this interference problem, it is now apparent that yet a new generation of nanofluidic chips need to be produced, using a silicon wafer with a thinner oxide layer as the substrate. Specifically, based on the calculations depicted in **Figure 19**, we opted for 200 nm oxide thickness, since this would minimize interference while at the same time leaving enough material to etch the 150 nm deep nanochannels. This new generation of nanofluidic chips also had additional features that I will explain in detail in chapter 2.4.2.2.

2.4.2.2 Upgrading the chip design to mitigate nanochannel clogging

While obviously being disappointing, I saw the necessity of fabricating a new generation of chips to mitigate the interference issue also as an opportunity to further modify and improve the fluidic design and add features that could be helpful when a chip is to be used for a longer time across many measurements and liquid exchanges. To motivate the added features I describe below, it is important to first discuss the main reason that a chip needs to be decommissioned and cannot be used for further experiments. This reason is that the nanochannels eventually get clogged by small debris particles that I have observed to be flushed into the system while handling the chip, the chuck, the pressure system and the syringes that I used to exchange the liquids. In fact, this "debris particle problem" can already be seen in the overview dark-field image in **Figure 18a**, where particles have accumulated in certain positions of the microchannels.

Since the exact origin(s) of these particles was unclear (and since they likely stem from different sources) we decided that instead of trying to avoid them completely, we would attempt to build a smart fluidic system that would prevent the particles from being flushed into the nanochannels. Specifically, I had discovered interesting solutions to similar challenges that are used within biological sciences[70–76]. Specifically, microfluidics systems used in this field often are equipped with solutions for different kinds of bacteria, cells or other biological particles that need to be sorted or separated. Since a high throughput is desired in these operations, they typically comprise microfabricated mechanical filters with pillar-like structures[72] or exploit the principle of hydrodynamic focusing. A detailed account of this principle would exceed the scope of this thesis but, in short, it is based on the behavior of particles in curved flows in confined fluidics. Depending on various parameters, such as fluid viscosity, flow speed and

particle size, the particles tend to accumulate at certain positions in the microchannel and can thereby be filtered out.

Inspired by one relatively simple system for hydrodynamic focusing that was presented by Gou et. al. I designed a meandering structure (**see Figure 20b**) in the inlet microchannels of my new chip that served the purpose of concentrating any larger particles in the middle of the liquid stream through the channel. Since a specifically designed and optimized microfluidic system for hydrodynamic focusing would have required in-depth knowledge of the fluid dynamics of the system and, most importantly (and impossible to get), details about the particles to be filtered, I estimated a "reasonable" geometry for the meandering structure where I made sure that it would mean no harm to the rest of the fluidic system if the hydrodynamic focusing would not work. Furthermore, I found it interesting and relevant to implement into the new design as proof of concept that highlights the fantastic opportunities provide by micro- and nanofluidics.

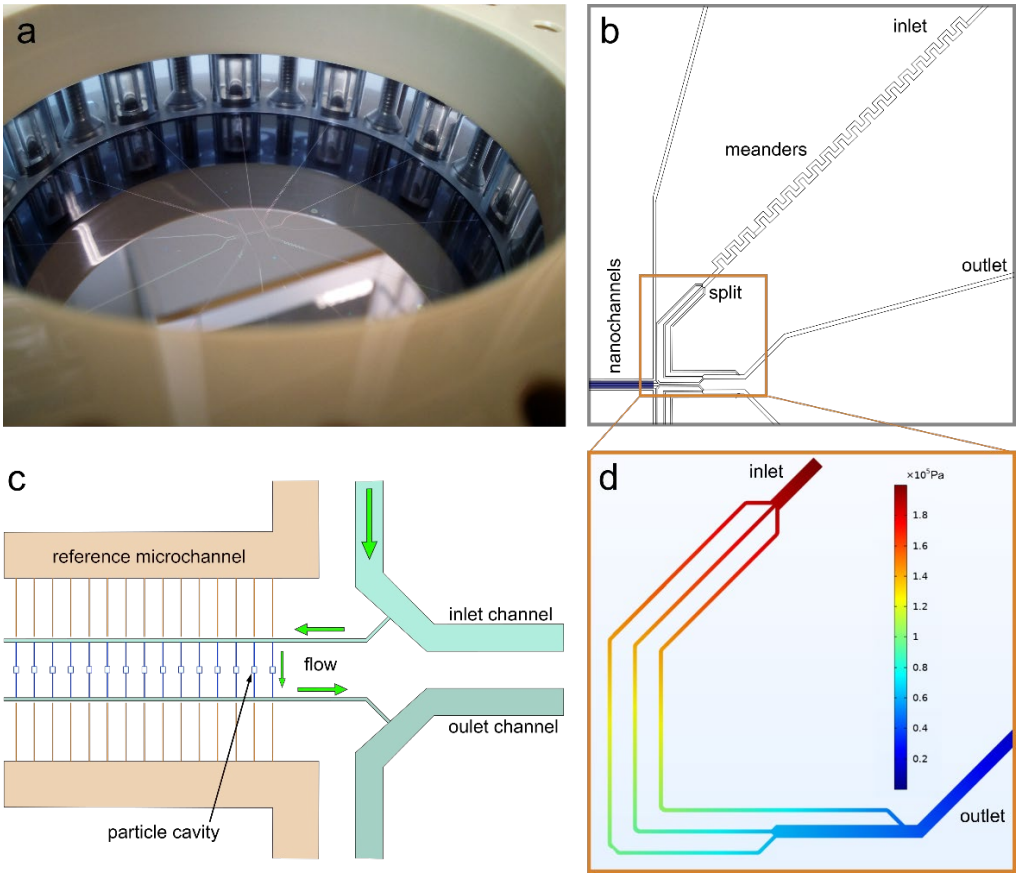

Figure 20. *a) Photograph of a nanofluidic wafer mounted in the chuck. The microchannel system is visible as brighter lines, leading from the reservoirs to the nanochannel area. The glass tubes connecting to the reservoirs are visible in the transparent perimeter of the chuck. b) Schematic overview of the redesigned microfluidic system of the new chip design. The rectangular meanders in the inlet channel are to focus the small "debris" particles in the liquid to the center of the flow, such that they are transported into the middle channel of the three-way split after the meander, and thereby are removed from the rest of the liquid further flowing towards the nanofluidic system. Accordingly, the access channels to the nanochannels are connected to the smaller left microchannel (labeled as inlet channel in c) of the three-way-split, where no particles should be present.*

*c) Drawing of the reaction nanochannel system, together with the reference nanochannels and in- and outlet microchannels adopted from the previous chip design (**cf.Figure 15**). The only difference is that the areas of the nanofluidic system that host Au nanoparticles have been extended and that there is now a total of 135 nanochannels in the system (see text for details). d) Comsol simulation of the split microchannel area that connects to the meanders that reveals the pressure gradient in the branched channels when the inlet is pressurized with 2 bar. As the key point, we see that it is very similar in all three split channels, which should guarantee a similar flow speed in the split channels and therefore an undisturbed separation of the particles from the rest of the liquid.*

The main idea behind my design is that the particles will stay closer to the inner radius of every curve of the meander when flowing around a corner according to a similar design by Gou et. al.[75] When exiting the meander-structure the particles would thereby be focused in the middle of the microchannel. Hence, if they at this point encounter a three-way junction that splits the microchannel, the center channel at the split would capture the particles and thus separate them from the liquid that is flushed towards the nanofluidic system via one of the other microchannels at the split. Corresponding Comsol Multiphysics simulations of the flow and pressure drop across the three microchannels after the split are depicted in **Figure 20d.** As the key point, they show that the pressure drop in all three split channels is identical, so that the flow speed is so as well, thereby enabling an undisturbed splitting and separation of the debris particles.

In addition to the meander system to mitigate clogging by dirt particles, the new chip generation also featured 135 nanochannels, where each channel was equipped with different particle constellations of Au and as a second metal also Pd. The particle(s) in sets of 1, 10 or 100 were placed in small cavities which were all 5.6 µm long and had three different widths of 0.4 µm, 0.7µm and 4 µm. The cavities served the purpose of prolonging the residence time of reactants close to the particle to increase conversion and thereby – hopefully – scattering contrast. In addition to the channels filled with particles the chip also features 45 empty nanochannels that would serve as negative controls.

2.4.2.3 Automatization of data acquisition

The large number of differently decorated nanochannels in terms of number and type of nanoparticles on my new chip design and my ambition to monitor up to 135 nanochannels in a single experiment made it clear that manual switching of pressures applied to the fluidic systems to redirect flow and of spectrometer settings would be challenging. Hence, I decided to write a LabView program that would carry out the measurements automatically. Furthermore, remote control enables more precise control of applied pressure and chip position on the microscope via the motorized stage and therefore creates more reproducible conditions between measurements.

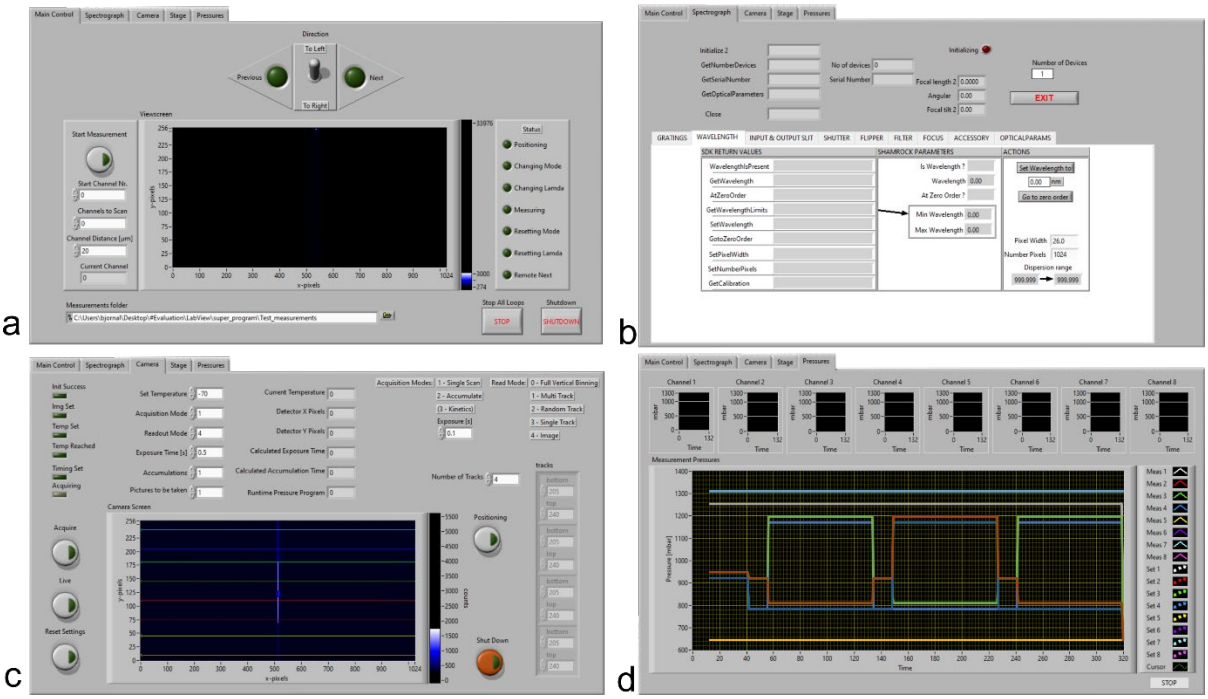

***Figure 21**. User interfaces for the LabView program that was written for the automatization of NSS measurements on a large number of parallel nanochannels. a) Main control interface, with settings for the number of channels to be measured, the distance between the channels and a control panel that shows the current step in the measurement, together with a screen showing the current camera image. b) Spectrometer interface, with settings for the grating/mirror. c) Camera interface with acquisition settings and the areas for recording the upper reference channel, the up- and downstream section of the reaction channel hosting the particle(s). d) Pressure control window, which would display the current applied pressure levels for each of the eight inlets.*

The program itself is structured into four parts, each being responsible for one connected instrument and each having its own user interface: (i) spectrograph, (ii) camera, (iii) pressure control, and (iv) microscope stage (**Figure 21**). To illustrate which steps were needed to record one complete data set from one nanochannel, I will give a short description in chronological order.

0. Setting up the microscope, connecting all required parts on the hardware and software level, filling the reservoirs with the respective solutions, and moving the first channel into position and focus, checking the camera acquisition settings and then starting the measurement in the software.

1. The program will first correct the position of the nanochannel in the field of view of the camera and regarding the slit of the spectrograph by detecting its vertical ends and the horizontal position of the center of the nanochannel image.

2. The spectrograph changes from the mirror to the grating with 150 l/mm, setting a predetermined center wavelength which was typically 642 nm.

3. Water is flushed through the nanochannels by applying pressure at the inlet of the microchannels that are connected the water-filled reservoir via the Fluidgent device.

Thereafter, the scattering intensity spectra of all four channel sections (upper and lower reference channel, Up- and downstream sections of the reaction channel) will be recorded and binned, such that each section has one scattering spectrum recorded. The spectra obtained at this stage, where all channels are filled with water, are needed to calibrate the reference for the later evaluation.

4. Now the reactants (Allura Red with $NaBH_4$ in water or H_2O_2 in water) were flushed in by applying a pressure of 2 bar to the inlet that contained the corresponding solution via the Fluidgent device, while the recording of the spectra continued. Depending on which flow situation was desired in the micro and nanofluidic system, all inlet and outlet pressures could be varied between 10 mbar and 7 bar.
5. The pressures were switched again, such that water was again flushed through the nanochannels from the water inlet via the respective microchannel. This step is included to clean the channels from reactants and to provide a comparison to step 3, as the situation should now be identical to the start.
6. Having completed one set of measurements for one channel, the grating in the spectrograph is replaced by the mirror, so that the image of the channel becomes visible again.
7. The stage is moved by the distance between channels, such that the next channel can be automatically positioned, and the process starts again at step 1 to acquire data from the next channel in the exact same manner.

Even tough designed for spectrally resolved NSS measurements from single nanochannels, given the accurate control over the setup the program provides, it can easily be modified to omit the spectral information and only record scattering intensity. The use and implementation of this automatization software did not only make all measurements comparable since the pressures and time steps were the same, but it also made the recording of larger and more diverse datasets possible, as it was the intention with the new chip design with 135 nanochannels of different configurations.

2.4.2.4 Nanoparticle catalysis – Allura Red and H_2O_2 on Au and Pd

As the first experiment with the latest generation of chips and the automated setup, I aimed at reproducing my previous results on degradation of Allura Red on Au nanoparticles (**cf. Figure 17**). For this purpose, I again prepared a 100 mM solution of the dye and mixed it with a 200 mM solution of $NaBH_4$. This mixed solution was subsequently pipetted into one reservoir connected to a microchannel inlet. Monitoring the scattering spectrum of a nanochannel with a 5.6 x 4 µm cavity and an arrangement of 100 gold particles with 50 nm diameter localized in the cavity produced the result shown in **Figure 22a** for three subsequent measurements, where the procedure described above was repeated for three times for the same channel.

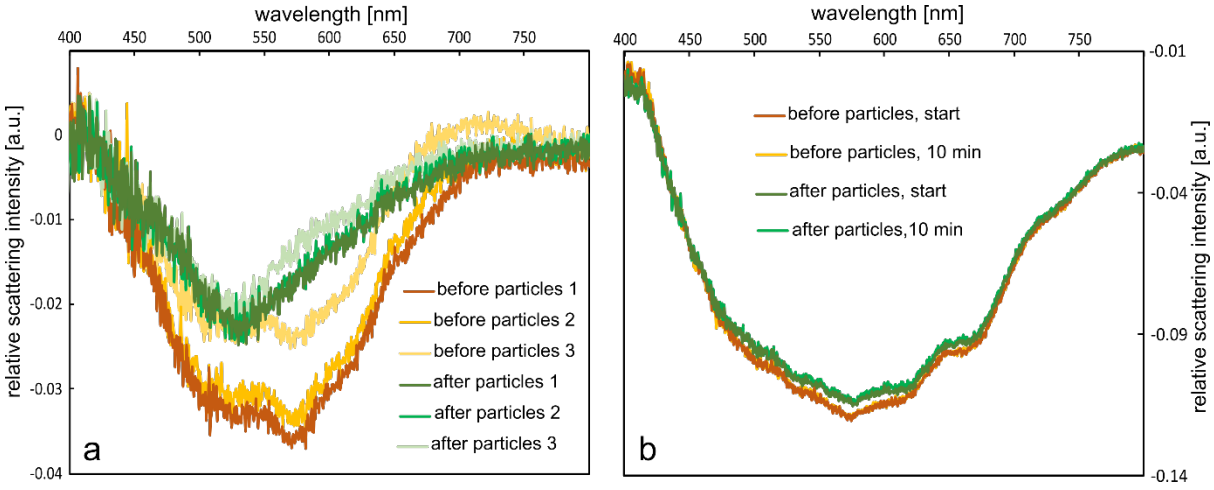

***Figure 22**. Referenced scattering intensity difference spectra for three subsequent measurements of catalytic decomposition of a 100 mM Allura Red solution by 200 mM $NaBH_4$ over hundred 50 nm Au nanoparticles in a nanofluidic channel. b) Referenced scattering intensity difference spectra acquired during the catalytic decomposition of 15 % H_2O_2 in water over hundred 50 nm Pd nanoparticles inside a nanofluidic channel.*

The improvement regarding the interference fringe pattern is evident, since it is essentially not noticeable in the spectra anymore. Consequently, the shape of the spectrum now also resembles more clearly the RI spectrum of Allura Red[60] with the broad double peak between 500 nm and 600 nm that is connected to the decrease of the absorption in this range (**see Figure 16a**). The reduced referenced scattering intensity difference downstream of the catalyst is again also clearly visible and indicates that the catalyst is decomposing the dye. The most prominent spectral feature that can be seen is that the peak at 575 nm has vanished in the downstream spectra. However, the downstream spectra still exhibit a distinctive peak at 530 nm, which could be indicative of an incomplete decomposition or that other products than those shown in **Figure 16b** have formed[77]. Finally, it is also interesting to see that the upstream scattering spectrum decreases over time during the three consecutive measurements, which could indicate that the dye degradation also takes place directly in solution, however at a much lower rate than on the Au catalyst. Therefore, as an intermediate summary, I was able to reproduce my previous results with Allura Red but this time without fringes, which significantly increased the level of detail that can be seen in the spectra.

Since in this latest chip design, I had decorated 50 % of the nanofluidic system with Pd particles to have a second catalyst at hand to also investigate a color-less reaction, I prepared a new

experiment using the catalytic decomposition of H_2O_2 on Pd as the model reaction. This reaction is quite well investigated[1,2,78–82] for various catalysts, and water and molecular oxygen are the products of the decomposition reaction. The correspondingly obtained result when flushing a 15% aqueous H_2O_2 solution over 100 Palladium particles with 50 nm diameter and in a cavity of the nanochannel that had the same size as for the Allura Red experiment discussed above is summarized in **Figure 22b**. As the key result, we see more or less featureless referenced scattering intensity difference spectra, in agreement with the lack of absorption bands of the reactants. As the second key observation I notice that, compared to the Allura Red case, the difference between up- and downstream spectra is very small. This either means that the sensitivity towards reaction induced RI changes in a colorless reaction is very small (which we from theory know is not the case) or that the catalytic activity of the Pd nanoparticles in the nanochannels is very low. To ensure that the small observed difference between the up- and downstream particles was not simply an artefact, we can compare the first measured spectrum with a spectrum obtained after running the reaction for 10 min. Clearly, we see that we essentially obtain the same result. This not only indicates that the measured difference likely is caused by the reaction but also highlights the excellent long-term stability of the setup thanks to all the made improvements and the on-chip referencing.

Before further investigating the – surprisingly – low activity of the Pd nanoparticles nanofabricated into the nanofluidic channels in chapter 2.6 below, I need to again comment on the clogging problem imposed by debris particles. Unfortunately, it turned out that despite the taken countermeasures with the meandering microchannels not all debris particles are captured and removed from the liquid stream that reaches the nanochannels. Therefore, also this latest chip generation clogged up after very few measurements only, which means that no repeated measurements necessary for generating statistically relevant data are possible. As a consequence, I also completely abandoned this type of fluidic chips and samples (for now), despite the highly promising preliminary results obtained, and the significant amount of time invested. The main reason for this decision is the fact that upon a detailed investigation of the origin of the debris particles summarized in chapter 2.5 below, it became obvious that a radically different design was necessary to resolve the problem.

2.5 Fluidic system clogging by debris particles

The problem of debris particles has been present already in the very first chips with water reference channels that I have used. For example, small amounts of these particles can be seen in the corners of the microfluidic channels in **Figure 18a**. As a key characteristic of this problem, the amount of debris in a fluidic system could vary over time from single small particles being flushed through the microchannels up to massive amounts that reminded of a snow storm, as shown in **Figure 23**. The origin of those particles was unclear for a long time, since I was dedicated to keep all solutions clean and used only Milli-Q water in the experiments. At the same time, any actively taken countermeasures, such as filters in front of the syringes, exchange of O-rings in the chuck from NBR to more chemically resistant FFKM or hydrodynamic focusing in the last generation of chips proved ineffective in the end. Furthermore, it also turned out to be impossible to completely remove particles from clogged channels by reversed long term flushing. In other words, the fluidic systems became unusable rather rapidly and irreversibly.

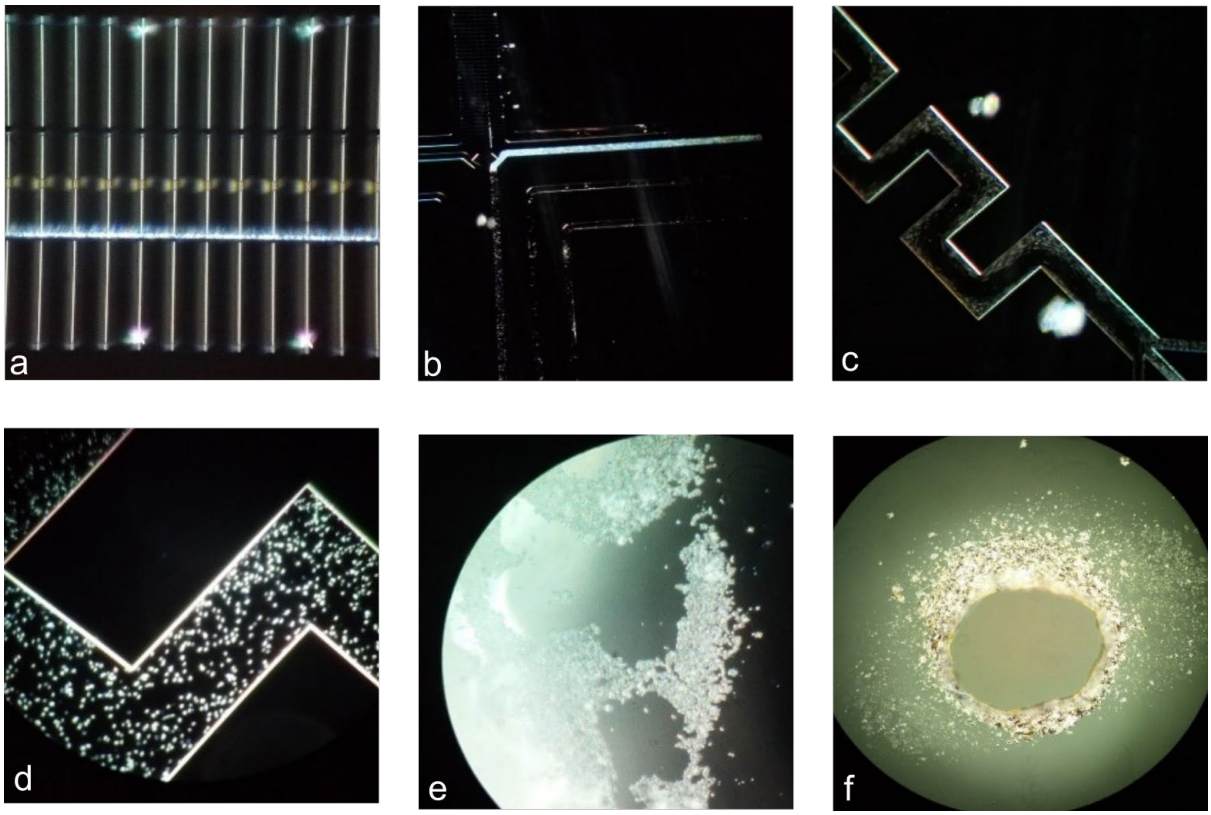

***Figure 23**. Debris particles as observed at various positions within the fluidic system in optical microscopy images. a) Debris particles in an access microchannel connecting to the array of reaction nanochannels. b) Debris particles in a microchannel. c) Debris particles in a meander channel under flow and d) at stagnant conditions. e) Debris particles accumulated at the bottom of the inlet hole. e) Bright-field optical microscope image of the sandblasted inlet hole in the glass lid that reveals its rough and cracked surface.*

Ultimately, after a detailed and systematic search for the origin of the debris particles, what remained were the sandblasted inlet holes in the glass lid that connect the reservoirs on the chip to the inlet system of the chuck. Corresponding SEM images I took from the hole area revealed that the walls of the cylindrical hole had a very rough structure (**Figure 24f and Figure 24a**). Furthermore SEM images of debris particles extracted from a chip revealed a structure reminiscent of shattered amorphous material (**Figure 24b,c**) with various shapes and sizes, where the smallest particles were in the size range of 100 nm to 200 nm (**Figure 24c**). Furthermore, I had observed that the largest number of particles occurred after a chip had not been used for a while, indicating that the debris had accumulated over time in the inlet holes.

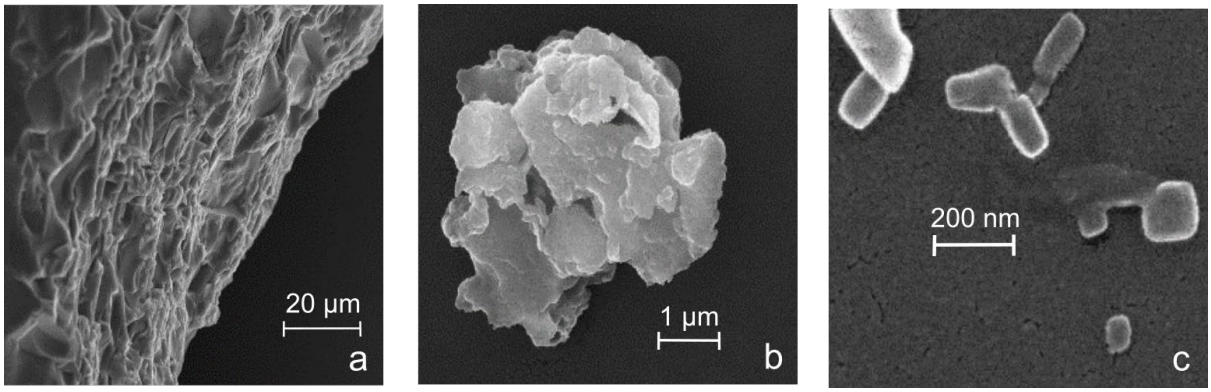

***Figure 24**. a) SEM image of the side wall of an inlet hole that was sandblasted through the Borofloat 33 cover glass used to seal the chip. b) and c) are SEM images of examples of particles found in the inlet holes.*

As a last aspect of relevance, I want to note that the behavior of the particles in the meanders was not of the kind expected for freely floating particles since they tended to accumulate where the flow speed was lowest rather than being focused in the center of the flow (**see Figure 23c**). This thus also hints at that these particles are heavy and in general behaved like "grit" in their tendency to accumulate in regions of low flow speed.

All this collected evidence thus leads to the conclusion that the origin of the debris particles most likely is the inlet holes in glass lid bonded onto the chip. This becomes particularly probable by the fact that this problem did not occur in my very first measurements, where I use the triangular chips (**Figure 9d**), in which the access holes were chemically etched though the silicon on the back side of the chip, rather than sandblasted through the glass. Since sandblasting is the only method we have at hand to drill small holes into glass, the only way to avoid the debris problem is to abandon the sophisticated chip design I have developed and return to simpler designs that enable access to the fluidic system from the silicon side of the wafer. This is what I have done in the part of my work that is described in detail in the appended manuscript and briefly summarized in chapter 3 below.

2.6 Investigating low Pd nanoparticle catalytic activity

Pd is a generally widely established catalyst for the decomposition of H_2O_2[1,80,81,83]. The more surprising was the apparently low activity of our nanofabricated Pd nanoparticles. To further investigate this issue, we nanofabricated arrays of Pd nanoparticles with sizes ranging from 10 nm to 100 nm on an open oxidized Si wafer surface using the same electron-beam nanofabrication recipe as used for the nanofluidic chips. In a first step, I cleaned the sample in a reducing 200 mM $NaBH_4$ solution to remove possible oxide. Subsequently, I immersed the sample in a 15% H_2O_2 solution by adding a drop on the surface (**Figure 25a**). After 5 minutes the formation of O_2 bubbles could be observed (**Figure 25b**). However, a more detailed analysis using dark-field scattering microscopy revealed that the bubbles were not forming at the positions of the Pd nanoparticle arrays but instead at the Pd number labels nanofabricated next to the nanoparticle arrays for their identification (**Figure 25d**).

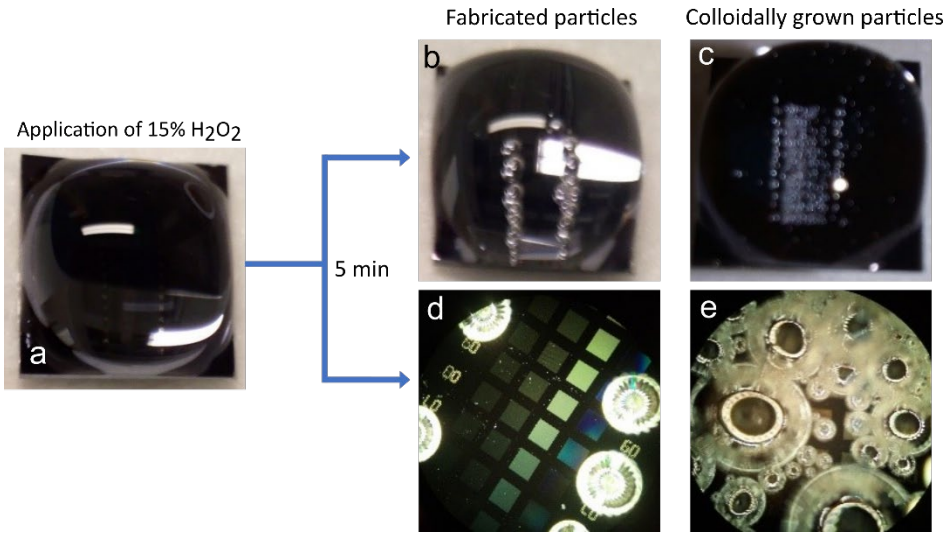

***Figure 25**. H_2O_2 decomposition reactivity tests of nanofabricated vs. colloidally grown Pd nanoparticles. a) A drop of 15% aqueous H_2O_2 solution is applied to an oxidized silicon wafer surface decorated with electron beam lithography nanofabricated arrays of Pd particles with different size. b) After 5 min incubation, the formation of O_2 bubbles is seen on a few areas of the sample. c) For a similar sample where the particles were grown in colloidal solution, a much more intense and evenly distributed O_2 bubble development is apparent. d) Dark-field microscopy reveals that bubble formation on the nanofabricated sample only occurs at the numbers labelling the arrays, not at the particle arrays themselves, whereas the colloidally grown particles in e) are highly active and induce intense bubble formation on the entire sample surface.*

This is a very puzzling result, which was further corroborated by repeating the same experiment but on a Si surface decorated with colloidally grown Pd nanoparticles, which indeed exhibited the expected high activity, as manifested in extensive formation of O_2 bubbles when exposed to the 15% H_2O_2 solution (**Figure 25c,e**). At this point, we do not understand the reason for the low activity of the nanofabricated Pd nanoparticles. We can only speculate that it, for example, may have to do with their structure. For example, it is known that (100) and (111) surfaces are important for high activity[1], which means that the low activity of our nanofabricated particles could be related to a lack of such surfaces. An alternative explanation is that residues from

nanofabrication, such as polymers used as evaporation masks, contaminate and deactivate the nanoparticle surface. As a consequence, in the last stage of my work that is described in the manuscript appended to this thesis and briefly summarized below, I have worked with colloidal Pt nanoparticles to overcome the unresolved activity problem of nanofabricated particles in the H_2O_2 decomposition reaction.

3 A new start

After the successful proofs of principle and systematic improvements together with the frustrating setbacks with my initial chip designs, it became clear that, to overcome the unresolved problems, I needed a fresh start with differently designed and fabricated fluidic chips and different nanoparticles. For this new start, I decided to focus on the H_2O_2 decomposition reaction due to its relevance in the current discussions about using it as fuel[84,85] and for H_2O_2 fuel cells[86,87]. Furthermore, from the method development perspective, it is the more interesting case since being able to monitor color- and fluorescence-free reactions is the "holy grail" in my field. That said, the demonstrated ability of spectrally resolved nanochannel scattering measurements that offer the potential to determine molecular fingerprints of molecules that exhibit absorption bands in the visible spectral range, is still highly interesting and I intend to pursue it at a later stage (see outlook). Secondly, due to experienced activity issues with nanofabricated particles, I decided to adopt the concept of trapping colloidal nanoparticles inside nanochannels that the group had developed recently[46].

3.1 A simplified chip design optimized for colloidal particle trapping

Inspired by the work of Levin et al.[46] and my encountered challenges with complex chips, we opted for a simplistic chip design only featuring two microchannels with a single set of nanochannels in between (**Figure 26**). This had the further key advantage that the connection to the inlet reservoirs was possible to etch chemically from the silicon side, thereby eliminating the debris particle problem. The dimensions of the nanochannels were chosen as before i.e., 150 nm x 150 nm cross section and a total length of 340 µm, whereof 170 µm would be visible in the field of view of the camera. As the key new feature that distinguishes them from all other designs presented in this thesis, they had a nanofabricated constriction in the center of each nanochannel (**Figure 27**). This constriction is designed to function as a physical trap for colloidal nanoparticles flushed through the nanochannel and corresponds to a 1 µm long section of the nanochannel along which the free height is reduced to 30 nm. Hence, any object larger than 30 nm cannot pass and will get trapped, while liquid flow through the nanochannel still is possible.

To work with these chips, since they featured the inlet holes on their backside, I had to use an inverted microscope to avoid the gravitation-induced leaking of liquid out of the chip. Specifically, I used a Zeiss Axio Observer Z1 inverted microscope, equipped with the same Thorlabs Solis 3C LED lamp that I had used before. The camera on this setup was a Andor iXon Ultra 888 EMCCD, which had the option to increase the sensitivity by activating an electron multiplier (EM) in front of the CCD chip. The chuck used for mounting the samples was similar to the one I used during my very first experiments (cf. **Figure 9d**) but had the additional feature that all four reservoirs could be accessed while the chip was mounted in the

chuck. This improved the workflow immensely since I did not have to unmount the chip for each exchange or refill of liquid.

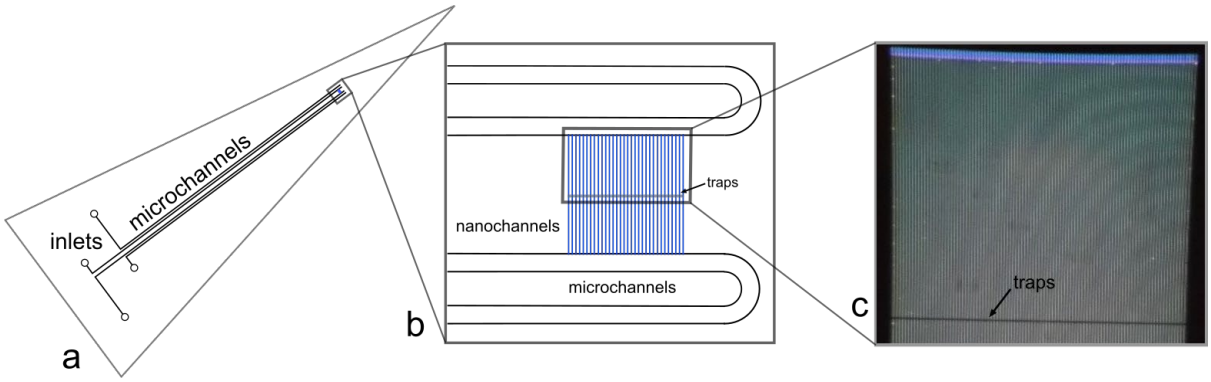

***Figure 26**. a) Schematic of the microfluidic in- and outlet system on the chip, designed for the trapping of colloidal particles. It is comprised of a parallel in- and outlet channel that connects to the set of nanofluidic channels on one end and to the inlet reservoirs on the other. The sketch is drawn with correct proportions. b) Schematic of the nanochannel region with the constriction traps in the middle of the nanochannels and the connections to the microchannels. c) Dark field scattering microscope image of the nanochannel set with 84 parallel channels in the field of view at 50 x magnification. Note the trap regions' darker appearance due to its reduced scattering intensity caused by the smaller channel dimensions at the constriction.*

3.2 Trapping colloidal Pt nanoparticles in nanochannels

As catalyst particles, I chose spherical Pt colloids with a nominal diameter of 70 nm comprised of small crystallites in the few nm size range (nanoComposix, PTCB70-10M, BioPure Platinum Nanoparticles – Bare (Citrate), 70 nm; **Figure 27c**). Pt is reported as an excellent catalyst for H_2O_2 decomposition, in par with or even exceeding Pd in terms of activity[81]. **Figure 27b,d** show SEM images of a single and multiple such Pt nanoparticle(s) captured by a nanochannel trap. These images were obtained from a special type of chip developed by Levin et al.[46], where the lid is reversibly attached using polysilsesquioxane (PSQ) to enable its reopening after particle trapping to enable the verification of trapped particles by electron microscopy.

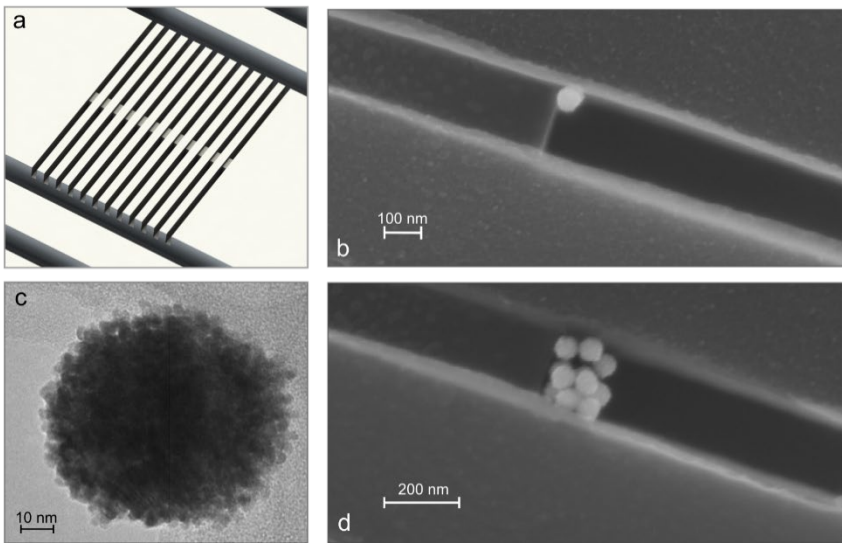

Figure 27. a) Artist's rendition of nanochannels with vertical constrictions in the center that serve as traps for colloidal nanoparticles flushed through the channels. b) SEM image of a constriction with a single trapped colloidal Pt particle. The image was enabled by using polysilsesquioxane (PSQ) to reversibly bond the lid to the chip, which enabled the reopening of the chip after particle trapping and thus imaging of the trap region. d) TEM image of a Pt particle. Note the very structured surface due to the particle being comprised of small crystallites in the few nm size range. d) SEM image of a trap at which 8-9 Pt particles have accumulated.

Since the re-openable chips with PSQ-bonded lids cannot be used for catalysis experiments due to leaking between nanochannels, I had to find an alternative way to verify and count Pt particle(s) trapped in each channel. This is of particular importance since we (i) aim at true single particle experiments and (ii) need to know the number of particles in each channel to be able to ultimately derive accurate reaction turnover frequencies. A particular complicating factor in this respect is that Pt nanoparticles are very weak scatterers, which, compared to Au, makes it impossible to directly see them in a dark field scattering image[88]. Interestingly, however, as discussed in detail in the appended manuscript, localizing the optically dark Pt nanoparticles inside nanofluidic channels makes them distinctly visible as dark spots with appropriate image post-processing (**Figure 28a-c**).

The first method that I have developed to see "dark" particles in the channels is by taking a reference picture of the empty channel system and subtracting it from the subsequent series of pictures in the trapping experiment. (**Figure 28a,b**). This method is straightforward, but it requires a very stable setup such that the reference picture remains valid for the entire experiment. The second method that does not require an empty channel reference is based on the fact that the nanochannels form a regular periodic pattern. Hence, by using a fast Fourier transform (FFT) bandpass filter and thereby eliminating the frequency belonging to the channel pattern from the picture, the particles appear as distinct dark spots since they do not periodically occur in the scattering images (**Figure 28c**). The drawback with the FFT approach is the relatively slow and computationally costly Fourier transformation. Hence, I have used the referencing method in my experiments.

With a method at hand to resolve single Pt nanoparticles inside my nanochannels, the next step was to find a way to quantitatively count them to know how many of them that would be

captured by each trap and thereby being able to optimize the trapping procedure towards as many single nanoparticles in each nanochannel as possible. In principle, there are two possibilities to do this. The first one relies on the fact that the particles are subject to Brownian motion, which means they will move randomly in front of the trap, provided no convective flow presses them against the trap. By simply monitoring the motion of the particles over time, I can count the number of particle peaks in the scattering trace along the nanochannel (**Figure 28d**). While in principle straightforward, this method requires that no particle gets stuck at the trap because it otherwise will not be counted. The alternative way to count trapped particles is to monitor the scattering intensity at the trap area of the channel since any Pt particle arriving there will reduce the scattering intensity in a stepwise manner (**Figure 28e**).

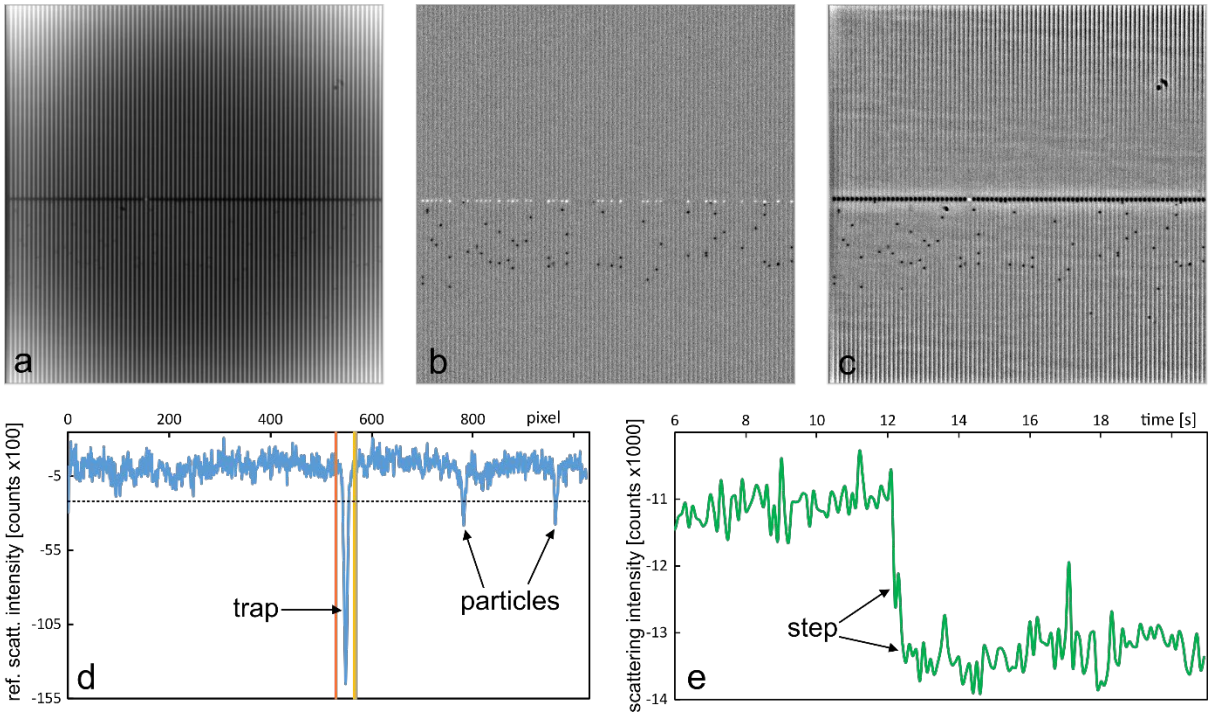

***Figure 28**. Single Pt colloidal particle detection and counting. a) Raw dark-field micrograph of an empty nanofluidic system. The dark line in the middle stems from the traps and the radial intensity gradient is the consequence of uneven illumination of the sample. b) Differential image obtained by subtracting an image of empty channels when the particles were pressed towards the trap by convective flow through the channel from an image where Pt particles are randomly diffusing inside the channel in absence of flow. This procedure reveals the particles as dark spots. Note that the white spots at the traps mark positions at which the particles were localized in the reference image. c) FFT version of the same image as in b). FFT reveals the particles since they are not part of the regular nanochannel pattern. d) Counting of freely diffusing particles by detecting their (negative) scattering signal along the nanochannel. e) Counting of nanoparticles at the trap by monitoring the change of the scattering intensity at the trap area over time. The arrival of a particle at the trap causes a steplike decrease in the scattering intensity.*

3.3 Summary of the appended manuscript

Equipped with the tools summarized above, I set out to study the catalytic decomposition of H_2O_2 on single trapped Pt colloidal particles and investigate the impact of two different types of ligands. This is the essence of the work described in the manuscript attached to this thesis. In summary, in this work I introduce the nanofluidic design that combines microchannels with nanochannels that feature a constriction to trap colloidal nanoparticles for nanofluidic scattering microscopy, NSM, of catalytic reactions. After discussing the theoretical background of Mie-scattering as the underlying principle for the scattering-based detection in nanochannels, a linear relation between H_2O_2 concentration in a single nanochannel and the scattered light intensity is established experimentally and verified theoretically. To subsequently demonstrate the potential of concentration measurements in nanochannels based on NSM, we quantitatively assess molecular diffusion of H_2O_2 and demonstrate that the bulk diffusion coefficient can be extracted from NSM measurements. As the next step, we demonstrate the trapping of 70 nm colloidal Pt nanoparticles in the nanochannels, and their counting based of differential imaging. As the final step, we then set out to investigate the H_2O_2 decomposition reaction on single trapped particles. For this purpose, we combine nanochannel scattering readout that informs about H_2O_2 concentration inside the channel, adjacent to the Pt particle during reaction, and the growth rate of O_2 bubbles formed in the channel from the reaction product. In this way, we can derive single particle turnover frequencies at kinetically controlled reaction conditions, as verified by the lack of gradient formation in H_2O_2 concentration in the nanochannel. We find a significant distribution of activity for individual particles which can be traced back to their broad size distribution. Applying this concept to identical Pt particles covered by two different types of ligands, i.e., citrate and Polyvinylpyrrolidone (PVP), we reveal that PVP coated single Pt nanoparticles exhibit a factor 2 lower reaction rate than citrate covered ones, likely due to a combination of larger steric hindrance by the long PVP molecules and their stronger bonding to both Pt terraces and edges. This highlights the impact of surfactant molecules on catalytic reactions and the potential of NSM to unravel them.

4 Summary and Conclusions

In the course of this thesis, I have developed a technique for the investigation of the catalytic activity of single nanoparticles that is based on the scattering of light from nanochannels that contain those particles and confine their reaction products – Nanofluidic Scattering Microscopy, NSM. The underlying physical principle is Mie-scattering from sub-wavelength objects, which connects the scattered intensity of light from a nanochannel to the difference in refractive index (RI) between the fluid in the channel and the surrounding material.

The introduction of a H_2O_2 solution into the nanochannels revealed a decrease in scattering intensity proportional to the refractive index of the solution. This first key result corroborated my theoretical findings that I had derived from Mie theory. Furthermore, I was able to show that compounds that exhibit a specific absorption spectrum in the visible regime, like the dyes Allura Red or Brilliant Blue, give rise to a characteristic scattering spectrum when introduced into the nanochannels that can be described by the Kramers-Kronig relation. This implies that NSM has the potential to be used to (i) identify the concentration of reactants in nanoscale systems via the intensity of the scattered light since it scales approximately linearly with the concentration, and (ii) identify the type of compound in the channel if the scattered light is resolved spectrally in a variant of NSM that we named nanochannels scattering spectroscopy (NSS).

By using catalytic nanoparticles localized inside a nanochannel, I was able to demonstrate the possibility of NSM and NSS to monitor reactions on these nanoparticles by measuring scattered light only. This was done for the degradation of Allura Red over Au nanoparticles by recording the scattering spectra before and after the particle in the direction of flow and identifying the decrease of characteristic peaks in the spectra that signaled the chemical conversion. In addition, I demonstrated that comparing scattered light intensity before and after a particle can be used to monitor its reactivity even when optically transparent reactants are involved. Here, I used the decomposition of H_2O_2 over colloidal Pt particles to show that the nanochannels can confine the reaction product and thereby make it measurable calculate ToFs for single nanoparticles. Furthermore, the application of NSM as method to monitor concentration changes over time inside a nanochannel enabled me to confirm that the reaction was taking place in the kinetically controlled regime since the reactant concentration at the particle position in the channel remained constant over time without developing any gradients. This demonstrates clearly how NSM can be used to assesses the reactivity of single particles directly by measuring the composition of the reactants and products via the intensity of the light scattered from the nanochannel.

Another key achievement was the possibility to detect and count optically dark colloidal nanoparticles via NSM as they were trapped in a nanochannel. This has the potential to pave the way for catalysis on single particles that are smaller than 10 nm and thus invisible in traditional dark field microscopy.

Finally, the development of the experimental setup that I have used for my experiments showed that special nanofluidic designs can help to increase NSM and NSS signal quality and long-term stability by providing an online reference in the form of isolated reference nanochannels.

In addition, the design of parallel nanochannels combined with the possibility of automated measurements enables a high throughput in the characterization of single particle catalysis.

In summary, the overarching and ultimate goal of my project, the assessment of the catalytic activity of single particles below 10 nm in size on the basis of optical microscopy and without the use of fluorescence markers or complex instrumentation, is now within reach and I have the knowledge and understanding that is necessary to make further progress towards this goal on my way to the PhD.

5 Outlook

The development of NSM and NSS for single particle catalysis has sparked a multitude of ideas that could be implemented to improve or extend its functionality. Among those are obviously the unfinished paths of the development where I consider the use of the spectral information to identify the type and concentration of reactants in a nanochannel as the maybe most important and interesting example. Here, studies of the degradation of dyes like Allura Red or Brilliant Blue that I have started but was unable to finish due to the debris problem seem very interesting. For their implementation, new chips that combine on-chip optical referencing with inlet holes etched from the silicon side need to be designed and nanofabricated.

As a second future direction, further developing the method towards studying colorless reactions, but without bubble formation, is very interesting. This will make NSM for single particle catalysis truly versatile by solely relying on the nanochannel scattering intensity approach that enables reactant concentration measurements in the channel. To further boost this approach, the spontaneous batch reactors described in the appended manuscript hint at a very interesting concept, namely, to develop ways to transiently open and close the nanochannels to create batch reactors with trapped single particles inside. The temporal evolution of changes in reactant concentration in this isolated volume can then be tracked via NSM or NSS to determine reactivity of the particle. As the key point, this batch approach would increase the resolution of the method since even slow reactions would with time create a measurable RI contrast. Following the same line, it likely would enable the study of smaller single particles, down to the sub-10 nm size regime, which is the one that is truly technically relevant.

From the perspective of setup modifications, I would like to revisit the reference channel concept, since it clearly improved signal quality and long-term stability by a good margin in my initial proof-of principle measurements. At the same time, the automatization program could be adapted to new measurement schemes to allow a more well-defined, reproducible, and facile acquisition of data.

In terms of the catalyst particle types studied it would be interesting to understand the difference between nanofabricated and colloidal particles in terms of their activity and structure since it is fundamentally interesting, despite having caused a change of direction during the development of this technique so far. One specifically interesting idea could be the colloidal overgrowth of nanoparticles onto nanofabricated seeds that have been placed in the nanochannels. This has been demonstrated on open surfaces[89] and would combine the best of two worlds, i.e., colloidal synthesis and nanofabrication. In this way, it could open new avenues for the investigation of structure-function correlations in catalysis at the single nanoparticle level.

As the final aspect, I want to highlight that it to date is not possible for us to structurally characterize the nanoparticles that are either nanofabricated or trapped inside a nanochannel. In other words, we know only from analogues investigated on open surfaces how they are expected to look like. While this is good enough for proof-of-principle experiments, if true single-particle structure function correlations are to be investigated with NSM and NSS, it is

critical that the particles in the channel can be structurally characterized before and after reaction. I predict that this could be possible by further developing the removable lid approach based on PSQ bonding (**cf. Figure 25**) in combination with SEM. If higher and ideally atomic resolution is targeted, TEM is the method of choice, which means that electron transparent membranes need to be integrated with the nanochannels. This appears to be within reach as nanochannel like devices are already in use in the field of in situ TEM to study materials in the liquid and gas phase[38,90,91].

6 Acknowledgements

I would like to acknowledge the funding provided by the Swedish Research Council and also thank the Knut and Alice Wallenberg Foundation for their support of the infrastructure in the MC2 nanofabrication laboratory at Chalmers.

There are many people that deserve my gratitude and that have provided the necessary assistance that I needed to stay on track but also to stay happy and healthy.

Of all people, it is my main supervisor Christoph that I need to thank, as I would not be in this fortunate situation that I am in now, since you accepted me into your group and gave me the opportunity to develop my ideas and myself as a person. Being now at the end of this licentiate thesis, thank you very much for helping me reach this point.

A big thanks goes out to Joachim, as he provided me with the necessary (fluidic) platform to conduct my research. I would like to see our conversations and regular exchange of chips to be continued.

Thanks to my examiner Henrik who gave me feedback on this thesis and keeping the Chemical Physics division together.

Thanks also to my office mate David for the fruitful discussions about everything and for letting me take care of his plant.

Thank you, Henrik KM for making sure that I returned from that place they call New York.

Thanks to Carl for providing the electron microscopy skills that gave this work an extra touch.

A big thanks in general to the whole Langhammer group and everyone at Chemical Physics for the private and professional discussions at the lunch table and the help provided.

A special thanks to Björn W who inspired me to take on a very interesting and wholesome hobby.

In the end, a big thanks to my family, I am forever in debt to your priceless advice. Thank you for supporting me in my career choices and making it possible to have a place of my own.

7 References

1. Plauck, A., Stangland, E. E., Dumesic, J. A. & Mavrikakis, M. Active sites and mechanisms for H2 O2 decomposition over Pd catalysts. *Proc. Natl. Acad. Sci. U. S. A.* **113**, E1973–E1982 (2016).

2. Serra-Maia, R. *et al.* Mechanism and Kinetics of Hydrogen Peroxide Decomposition on Platinum Nanocatalysts. *ACS Appl. Mater. Interfaces* **10**, 21224–21234 (2018).

3. Gao, W., Hood, Z. D. & Chi, M. Interfaces in Heterogeneous Catalysts: Advancing Mechanistic Understanding through Atomic-Scale Measurements. *Acc. Chem. Res.* **50**, 787–795 (2017).

4. Sambur, J. B. & Chen, P. Approaches to single-nanoparticle catalysis. *Annu. Rev. Phys. Chem.* **65**, 395–422 (2014).

5. Xu, W., Zhang, Y. & Chen, T. *Single particle nanocatalysis: Fundamentals and applications*. *Single Particle Nanocatalysis: Fundamentals and Applications* (2019). doi:10.1002/9783527809721.

6. Zhou, X., Choudhary, E., Andoy, N. M., Zou, N. & Chen, P. Scalable Parallel Screening of Catalyst Activity at the Single-Particle Level and Subdiffraction Resolution. *ACS Catal.* **3**, 1448–1453 (2013).

7. Hansen, T. W. & Wagner, J. B. Catalysts under Controlled Atmospheres in the Transmission Electron Microscope. *ACS Catal.* **4**, 1673–1685 (2014).

8. Hartman, T., Geitenbeek, R. G., Wondergem, C. S., van der Stam, W. & Weckhuysen, B. M. Operando Nanoscale Sensors in Catalysis: All Eyes on Catalyst Particles. *ACS Nano* **14**, 3725–3735 (2020).

9. Hartman, T., Wondergem, C. S., Kumar, N., van den Berg, A. & Weckhuysen, B. M. Surface- and Tip-Enhanced Raman Spectroscopy in Catalysis. *J. Phys. Chem. Lett.* **7**, 1570–1584 (2016).

10. Fam, Y. *et al.* A versatile nanoreactor for complementary in situ X-ray and electron microscopy studies in catalysis and materials science. *J. Synchrotron Radiat.* **26**, 1769–1781 (2019).

11. Hartman, T., Geitenbeek, R. G., Wondergem, C. S., Van Der Stam, W. & Weckhuysen, B. M. Operando Nanoscale Sensors in Catalysis: All Eyes on Catalyst Particles. *ACS Nano* (2020) doi:10.1021/acsnano.9b09834.

12. Meirer, F. & Weckhuysen, B. M. Spatial and temporal exploration of heterogeneous catalysts with synchrotron radiation. *Nat. Rev. Mater.* **3**, 324–340 (2018).

13. Cordes, T. & Blum, S. A. Opportunities and challenges in single-molecule and single-particle fluorescence microscopy for mechanistic studies of chemical reactions. *Nat. Chem.* **5**, 993–999 (2013).

14. Zhou, X. *et al.* Quantitative super-resolution imaging uncovers reactivity patterns on single nanocatalysts. *Nat. Nanotechnol.* **7**, 237–241 (2012).

15. Chen, P. *et al.* Spatiotemporal catalytic dynamics within single nanocatalysts revealed by single-molecule microscopy. *Chem. Soc. Rev.* **43**, 1107–1117 (2014).

16. Andoy, N. M. *et al.* Single-Molecule Catalysis Mapping Quantifies Site-Specific Activity and Uncovers Radial Activity Gradient on Single 2D Nanocrystals. *J. Am. Chem. Soc.* **135**, 1845–1852 (2013).

17. Alekseeva, S., Nedrygailov, I. I. & Langhammer, C. Single Particle Plasmonics for Materials Science and Single Particle Catalysis. *ACS Photonics* **6**, 1319–1330 (2019).

18. Albinsson, D. *et al.* Copper catalysis at operando conditions—bridging the gap between single nanoparticle probing and catalyst-bed-averaging. *Nat. Commun.* **11**, 4832 (2020).

19. Liu, S. *et al.* In Situ Plasmonic Nanospectroscopy of the CO Oxidation Reaction over Single Pt Nanoparticles. *ACS Nano* **13**, 6090–6100 (2019).

20. Albinsson, D. *et al. Operando* detection of single nanoparticle activity dynamics inside a model pore catalyst material. *Sci. Adv.* **6**, eaba7678 (2020).

21. Albinsson, D. *et al.* Shedding Light on CO Oxidation Surface Chemistry on Single Pt Catalyst Nanoparticles Inside a Nanofluidic Model Pore. *ACS Catal.* **11**, 2021–2033 (2021).

22. Larsson, E. M., Langhammer, C., Zorić, I. & Kasemo, B. Nanoplasmonic Probes of Catalytic Reactions. *Science (80-.).* **326**, 1091–1094 (2009).

23. Dahlin, A. B., Tegenfeldt, J. O. & Höök, F. Improving the Instrumental Resolution of Sensors Based on Localized Surface Plasmon Resonance. *Anal. Chem.* **78**, 4416–4423 (2006).

24. Taylor, A. B. & Zijlstra, P. Single-Molecule Plasmon Sensing: Current Status and Future Prospects. *ACS Sensors* **2**, 1103–1122 (2017).

25. Etchegoin, P. G. & Le Ru, E. C. A perspective on single molecule SERS: Current status and future challenges. *Phys. Chem. Chem. Phys.* **10**, 6079–6089 (2008).

26. Ding, S. Y., You, E. M., Tian, Z. Q. & Moskovits, M. Electromagnetic theories of surface-enhanced Raman spectroscopy. *Chem. Soc. Rev.* **46**, 4042–4076 (2017).

27. van Schrojenstein Lantman, E. M., Deckert-Gaudig, T., Mank, A. J. G., Deckert, V. & Weckhuysen, B. M. Catalytic processes monitored at the nanoscale with tip-enhanced Raman spectroscopy. *Nat. Nanotechnol.* **7**, 583–586 (2012).

28. Langhammer, C., Larsson, E. M., Kasemo, B. & Zorić, I. Indirect Nanoplasmonic Sensing: Ultrasensitive Experimental Platform for Nanomaterials Science and Optical Nanocalorimetry. *Nano Lett.* **10**, 3529–3538 (2010).

29. Dong, J.-C. *et al.* Direct In Situ Raman Spectroscopic Evidence of Oxygen Reduction Reaction Intermediates at High-Index Pt(hkl) Surfaces. *J. Am. Chem. Soc.* **142**, 715–719 (2020).

30. Swearer, D. F. *et al.* Heterometallic antenna-reactor complexes for photocatalysis. *Proc. Natl. Acad. Sci. U. S. A.* **113**, 8916–8920 (2016).

31. Antosiewicz, T. J., Wadell, C. & Langhammer, C. Plasmon-Assisted Indirect Light Absorption Engineering in Small Transition Metal Catalyst Nanoparticles. *Adv. Opt. Mater.* **3**, 1591–1599 (2015).

32. Zhou, L. *et al.* Light-driven methane dry reforming with single atomic site antenna-reactor plasmonic photocatalysts. *Nat. Energy* **5**, 61–70 (2020).

33. Vadai, M., Angell, D. K., Hayee, F., Sytwu, K. & Dionne, J. A. In-situ observation of plasmon-controlled photocatalytic dehydrogenation of individual palladium nanoparticles. *Nat. Commun.* **9**, 1–8 (2018).

34. Dunn, G. *et al.* Graphene-Sealed Flow Cells for in Situ Transmission Electron Microscopy of Liquid Samples. *ACS Nano* **14**, 9637–9643 (2020).

35. van der Wal, L. I., Turner, S. J. & Zečević, J. Developments and advances inin situtransmission electron microscopy for catalysis research. *Catal. Sci. Technol.* **11**, 3634–3658 (2021).

36. Yokosawa, T., Alan, T., Pandraud, G., Dam, B. & Zandbergen, H. In-situ TEM on (de)hydrogenation of Pd at 0.5-4.5bar hydrogen pressure and 20-400°C. *Ultramicroscopy* **112**, 47–52 (2012).

37. Giorgio, S. *et al.* Environmental electron microscopy (ETEM) for catalysts with a closed E-cell with carbon windows. *Ultramicroscopy* **106**, 503–507 (2006).

38. Creemer, J. F. *et al.* Atomic-scale electron microscopy at ambient pressure. *Ultramicroscopy* **108**, 993–998 (2008).

39. Williamson, M. J., Tromp, R. M., Vereecken, P. M., Hull, R. & Ross, F. M. Dynamic microscopy of nanoscale cluster growth at the solid-liquid interface. *Nat. Mater.* **2**, 532–536 (2003).

40. Kraus, T. & de Jonge, N. Dendritic Gold Nanowire Growth Observed in Liquid with Transmission Electron Microscopy. *Langmuir* **29**, 8427–8432 (2013).

41. Vendelbo, S. B. *et al.* Visualization of oscillatory behaviour of Pt nanoparticles catalysing CO oxidation. *Nat. Mater.* **13**, 884–890 (2014).

42. Ghosh, T. *et al.* Periodic structural changes in shape-controlled Pd nanoparticles during oscillatory CO oxidation. *Submitted* 1–10 (2022) doi:10.1038/s41467-022-33304-x.

43. Boyes, E. D., Lagrow, A. P., Ward, M. R., Mitchell, R. W. & Gai, P. L. Single Atom Dynamics in Chemical Reactions. *Acc. Chem. Res.* (2020) doi:10.1021/acs.accounts.9b00500.

44. Bacsa, W., Bacsa, R. & Myers, T. Microscopic Origin of the Index of Refraction. in *Optics Near Surfaces and at the Nanometer Scale* 65–83 (Springer International Publishing, 2020). doi:10.1007/978-3-030-58983-7_5.

45. Levin, S. *et al.* A nanofluidic device for parallel single nanoparticle catalysis in solution. *Nat. Commun.* **10**, (2019).

46. Levin, S. *et al.* Nanofluidic Trapping of Faceted Colloidal Nanocrystals for Parallel Single-Particle Catalysis. *ACS Nano* **16**, 15206–15214 (2022).

47. Špačková, B. *et al.* Label-free nanofluidic scattering microscopy of size and mass of single diffusing molecules and nanoparticles. *Nat. Methods* **19**, 751–758 (2022).

48. Swapnasrita, S. *et al.* Unravelling CO oxidation reaction kinetics on single Pd nanoparticles in nanoconfinement using a nanofluidic reactor and DSMC simulations. *Chem. Eng. Sci. X* **9**, 100088 (2021).

49. Sliney, D. H. What is light? the visible spectrum and beyond. *Eye* **30**, 222–229 (2016).

50. Bohren, C. F. & Huffman, D. R. Rayleigh-Gans Theory. *Absorpt. Scatt. Light by Small Part.* 158–165 (2007) doi:10.1002/9783527618156.ch6.

51. Sai, T., Saba, M., Dufresne, E. R., Steiner, U. & Wilts, B. D. Designing Refractive Index Fluids using the Kramers – Kronig Relations – Supplementary Information. *Faraday Discuss.* 1–4 (2020).

52. Kramers-Kronig Relations and Sum Rules in Linear Optics. in *Kramers-Kronig Relations in Optical Materials Research* 27–48 (Springer Berlin Heidelberg, 2005). doi:10.1007/3-540-27316-6_4.

53. Albinsson, D. *Combining nanoplasmonics and nanofluidics for single particle catalysis*. *Licentiate Thesis* (2018).

54. Thoms, L., Girwidz, R. & Munich, L. M. U. Experimenting from a Distance : Optical Spectrometry via the Internet. *MPTL18 – B. Proc.* 59–63 (2013).

55. Pope, R. M. & Fry, E. S. Absorption spectrum (380–700 nm) of pure water II Integrating cavity measurements. *Appl. Opt.* **36**, 8710 (1997).

56. Molina, L. T., Schinke, S. D. & Molina, M. J. Sist I of of and of. **4**, 80–82 (1977).

57. Malitson, I. H. Interspecimen Comparison of the Refractive Index of Fused Silica. *J. Opt. Soc. Am.* **55**, 1205–1209 (1965).

58. Bashkatov, A. N. & Genina, E. A. Water refractive index in dependence on temperature and wavelength: A simple approximation. *Proc. SPIE* 393–395 (2003) doi:10.1117/12.518857.

59. Giguère, P. A. & Geoffrion, P. REFRACTIVE INDEX OF HYDROGEN PEROXIDE SOLUTIONS. A REVISION. *Can. J. Res.* **27b**, 168–173 (1949).

60. Sai, T., Saba, M., Dufresne, E. R., Steiner, U. & Wilts, B. D. Designing refractive index fluids using the Kramers-Kronig relations. *Faraday Discuss.* **223**, 136–144 (2020).

61. Esmaeili, S. *et al.* Degradation products of the artificial azo dye, Allura red, inhibit esterase activity of carbonic anhydrase II: A basic in vitro study on the food safety of the colorant in terms of enzyme inhibition. *Food Chem.* **213**, 494–504 (2016).

62. Salem, M. A., Al-Ghonemiy, A. F. & Zaki, A. B. Photocatalytic degradation of Allura red and Quinoline yellow with Polyaniline/TiO2 nanocomposite. *Appl. Catal. B Environ.* **91**, 59–66 (2009).

63. Lin, C., Tao, K., Hua, D., Ma, Z. & Zhou, S. Size effect of gold nanoparticles in catalytic reduction of p-nitrophenol with NaBH4. *Molecules* **18**, 12609–12620 (2013).

64. Salem, M. A., Abdel-Halim, S. T., El-Sawy, A. E. H. M. & Zaki, A. B. Kinetics of degradation of allura red, ponceau 4R and carmosine dyes with potassium ferrioxalate complex in the presence of H2O2. *Chemosphere* **76**, 1088–1093 (2009).

65. Torres-Pérez, J., Medellín-Castillo, N. & Reyes-López, S. Y. α and γ Alumina Spheres for Azo Dye (Allura Red) Removal from Aqueous Media. *Adsorpt. Sci. Technol.* **2022**, (2022).

66. Ansar, S. M. *et al.* Removal of Molecular Adsorbates on Gold Nanoparticles Using Sodium Borohydride in Water. *Nano Lett.* **13**, 1226–1229 (2013).

67. Neal, R. D., Inoue, Y., Hughes, R. A. & Neretina, S. Catalytic Reduction of 4-Nitrophenol by Gold Catalysts: The Influence of Borohydride Concentration on the Induction Time. *J. Phys. Chem. C* **123**, 12894–12901 (2019).

68. Gungor, T., Gungor, E. & Saka, B. Fast and interference fringe independent optical characterization of zinc oxide nano thin films using model-based genetic algorithm for optoelectronic applications. *Nanomater. Nanotechnol.* **6**, 1–7 (2016).

69. Aspnes, D. E. & Studna, A. A. Dielectric functions and optical parameters of Si, Ge, GaP, GaAs, GaSb, InP, InAs, and InSb from 1.5 to 6.0 eV. *Phys. Rev. B* **27**, 985–1009 (1983).

70. Zhou, Y., Ma, Z., Tayebi, M. & Ai, Y. Submicron Particle Focusing and Exosome Sorting by Wavy Microchannel Structures within Viscoelastic Fluids. *Anal. Chem.* **91**, 4577–4584 (2019).

71. Bhagat, A. A. S., Kuntaegowdanahalli, S. S. & Papautsky, I. Continuous particle separation in spiral microchannels using dean flows and differential migration. *R. Soc. Chem.* **8**, 1906–1914 (2008).

72. Chiu, Y. Y., Huang, C. K. & Lu, Y. W. Enhancement of microfluidic particle separation using cross-flow filters with hydrodynamic focusing. *Biomicrofluidics* **10**, (2016).

73. Cruz, F. J. & Hjort, K. High pressure inertial focusing for separation and concentration of bacteria at high throughput. *J. Phys. Conf. Ser.* **922**, (2017).

74. Fouet, M. *et al.* Filter-less submicron hydrodynamic size sorting. *R. Soc. Chem.* **16**, 720–733 (2016).

75. Gou, Y., Jia, Y., Wang, P. & Sun, C. Progress of inertial microfluidics in principle and application. *Sensors (Switzerland)* **18**, (2018).

76. Ahmed, T., Shimizu, T. S. & Stocker, R. Microfluidics for bacterial chemotaxis. *Integr. Biol.* **2**, 604–629 (2010).

77. Gosetti, F. *et al.* Identification of photodegradation products of Allura Red AC (E129) in a beverage by ultra high performance liquid chromatography-quadrupole-time-of-flight mass spectrometry. *Anal. Chim. Acta* **746**, 84–89 (2012).

78. Hart, A. B. & Ross, R. A. Catalytic Decomposition of Hydrogen Peroxide Vapour by Equimolar Mixed Oxides. *Nature* **193**, 1175–1177 (1962).

79. Robbins, J. P. *et al.* Dependence of Hydrogen Peroxide Decomposition on the Size of Catalytic Gold Nanoparticles. 2 (2016).

80. Aeta, E. Peroxide Solutions on Platinum , Iridium , Palladium and Gold Surfaces *. *Solutions* **7**, 457–473 (1962).

81. Bianchi, G., Mazza, F. & Mussini, T. Catalytic decomposition of acid hydrogen peroxide solutions on platinum, iridium, palladium and gold surfaces. *Electrochim. Acta* **7**, 457–473 (1962).

82. Liu, J., Wei, X., Wang, X. & Liu, X. W. High-yield synthesis of ultrathin silica-based nanosheets and their superior catalytic activity in H2O2 decomposition. *Chem. Commun.* **47**, 6135–6137 (2011).

83. Menegazzo, F., Signoretto, M., Ghedini, E. & Strukul, G. Looking for the "dream catalyst" for hydrogen peroxide production from hydrogen and oxygen. *Catalysts* **9**, (2019).

84. Disselkamp, R. S. Energy Storage using Aqueous Hydrogen Peroxide. *Energy & Fuels* **22**, 2771–2774 (2008).

85. McDonnell-Worth, C. J. & MacFarlane, D. R. Progress towards direct hydrogen peroxide fuel cells (DHPFCs) as an energy storage concept. *Aust. J. Chem.* **71**, 781–788 (2018).

86. Chen, W. & Qu, B. Investigation of a platinum catalyst supported on a hydrogen peroxide-treated carbon black. *Int. J. Hydrogen Energy* **35**, 10102–10108 (2010).

87. Yi, L. *et al.* Carbon-Supported Bimetallic Platinum–Iron Nanocatalysts: Application in Direct Borohydride/Hydrogen Peroxide Fuel Cell. *ACS Sustain. Chem. Eng.* **6**, 8142–8149 (2018).

88. Langhammer, C., Kasemo, B. & Zorić, I. Absorption and scattering of light by Pt, Pd, Ag, and Au nanodisks: Absolute cross sections and branching ratios. *J. Chem. Phys.* **126**, (2007).

89. Preston, A. S., Hughes, R. A., Demille, T. B., Rey Davila, V. M. & Neretina, S. Dewetted nanostructures of gold, silver, copper, and palladium with enhanced faceting. *Acta Mater.* **165**, 15–25 (2019).

90. Van Omme, J. T. *et al.* Liquid phase transmission electron microscopy with flow and temperature control. *J. Mater. Chem. C* **8**, 10781–10790 (2020).

91. Pu, S., Gong, C. & Robertson, A. W. Liquid cell transmission electron microscopy and its applications. *R. Soc. Open Sci.* **7**, (2020).